1-1-2005

From the ashes of the mysterious core helium flash: Whole Earth Telescope observations of the pulsating subdwarf B star PG0014+067

Maja Vučković
Iowa State University

From the ashes of the mysterious core helium flash:

Whole Earth Telescope observations of the pulsating subdwarf B star

PG0014+067

by

Maja Vučković

A thesis submitted to the graduate faculty

in partial fulfillment of the requirements for the degree of

MASTER OF SCIENCE

Major: Astrophysics

Program of Study Committee:
Steven D. Kawaler, Major Professor
Igor A. Beresnev
Charles Kerton
Curt Struck

Iowa State University

Ames, Iowa

2005

Graduate College
Iowa State University

This is to certify that the master's thesis of

Maja Vučković

has met the thesis requirements of Iowa State University

Signatures have been redacted for privacy

DEDICATION

I would like to dedicate this thesis to all those who were, are, and will become able to spread their wings beyond the boundaries.

"Observation, not age, brings wisdom."

Publilius Syrus

TABLE OF CONTENTS

LIST OF TABLES vii

LIST OF FIGURES viii

ACKNOWLEDGEMENTS xii

ABSTRACT xiii

CHAPTER 1. The last frontier of evolutionary models of an ordinary star: exploring the consequences of the helium core flash 1

1.1 Life of an ordinary star: the art of change 2

1.1.1 Quiet helium ignition and beyond 2

1.1.2 The Helium core flash and beyond 4

1.2 Subdwarf B stars 6

1.2.1 General properties of subdwarf B stars 6

1.2.2 Pulsating sdB stars 10

1.3 Goal of this work 14

CHAPTER 2. Asteroseismology - methods and tools 16

2.1 Terminology and Basic Physics 17

2.2 High speed photometry 20

2.2.1 PMT detectors 21

2.2.2 2-dimensional Charge Coupled Devices: CCD detectors 21

2.3 Photometric Issues 22

2.3.1 Noise 22

2.3.2 Aliases 24
2.4 Reduction Techniques 26
2.4.1 Reduction of PMT data 27
2.4.2 Reduction of CCD data 29
CHAPTER 3. Whole Earth Telescope observations of PG0014+067 . 32
3.1 Telescope allocations and weather 33
3.2 Observing Techniques 35
3.3 Data reduction 37
CHAPTER 4. The frequencies of PG0014+067 41
4.1 Summary of previous observations of PG0014+067 41
4.2 Frequency analysis of the WET data set on PG 0014+067 42
4.3 Weighting 46
4.4 Down to the beat - isolating the pulsations from the light curve of PG 0014 47
4.5 Conclusions 51
CHAPTER 5. Summary and discussion 65
5.1 Stability of the modes 65
5.2 Pattern analysis 71
5.2.1 Numerology 72
5.2.2 Equal spacings 73
5.3 Can we explain all this? 76
5.4 Summary 79
BIBLIOGRAPHY 82

LIST OF TABLES

Table 2.1 Characteristics of the CCD detectors used in Xcov24 on PG0014+067. 24

Table 3.1 Participating sites in Xcov24. 34

Table 3.2 Journal of observations : Xcov24 data on PG 0014. Runs marked with asterisks were not used in the final analysis due to the bad signal to noise ratio. 40

Table 4.1 Periodicities found in WET data on PG0014+067. 51

Table 4.2 Marginal detections- peaks with the amplitude between $3.7\sigma_{noise}$ and $3\sigma_{noise}$ seen in WET data on PG0014. 52

Table 4.3 Periodicities identified by Brassard et al. (2001) data on PG0014+067- taken from Table 2 of their paper. The column **Note** compares it with the WET data, with the frequencies listed in bold corresponding to our Table 4.1. 53

Table 5.1 Possible splittings found in the WET data set on PG0014. 72

Table 5.2 Spacings in PG 0014+067 from the WET run alone. 74

Table 5.3 Spacings in PG 0014+067, including extra peaks from ULTRACAM. 76

Table 5.4 Final fit to secure modes in PG 0014+067, including the modes found in ULTRACAM data, with δ=90.37 μHz, Δ = 101.22 μHz and with ν_{in}= 5923.24 μHz. 78

LIST OF FIGURES

Figure 1.1 HR diagram with the evolutionary path of a $1.5M_{\odot}$, with the mass of the remnant (after the gap) of $0.48M_{\odot}$. 5

Figure 1.2 HR diagram of a globular cluster M15, pin-pointing the HB and EHB stages of the evolution. The insert shows the optical image of M15. 7

Figure 1.3 Schematic HR diagram illustrating the instability strips. 11

Figure 1.4 $\log g - T_{\rm eff}$ diagram with the observed sdBV stars. The theoretical evolutionary thacks are included (after Kawaler & Hostler 2005). 12

Figure 2.1 Two single site runs (lulin-0008 and lulin-0010 with the average length of $\approx$ 7 hours) on PG0014+067 taken in two consecutive days obtained during Xcov 24- centered near the main frequency. The first panel shows the spectral window. 25

Figure 2.2 Seven runs on PG0014+067 taken during Xcov 24: sara213, sara214, lulin-0001, NOT-001, lulin-0008, lulin-0010 and maja10192004. Top panel shows the window. 27

Figure 2.3 A sample of a PMT run on PG0014 obtained during Xcov 24 . . 29

Figure 2.4 A sample of a CCD run on PG0014 obtained during Xcov 24. . . 31

Figure 3.1 Finder chart for PG0014+067 together with all possible comparison stars used. 36

Figure 3.2 Light curve for data on PG0014 obtained during Xcov 24. 39

Figure 4.1 Weighted Fourier transform of the complete WET data set on PG0014+067. 44

Figure 4.2 Spectral window for the PG0014+067 WET data set. 45

Figure 4.3 Weighted FT of the PG0014 WET data expanded to the region of the most power. 55

Figure 4.4 Upper panel: weighted FT of the full data set on PG0014 in the range of the most power. Lower panel: "unweighted" FT of the same data set at the same scale. 56

Figure 4.5 Top panel: the spectral window centered at 7000μHz given on the same frequency scale as the data. Middle panel: the FT of the entire WET data set on PG0014 expanded around the highest power. Bottom panel: the residual FT prewhitened by f_1 and f_2 all on the same frequency scale. Note the different amplitude scale. 57

Figure 4.6 Top panel: the prewhitened FT by f_1 and f_2. Bottom panel: the residual FT after removing the additional two modes, f_3 and f_4. Note the different amplitude scale. 58

Figure 4.7 Top panel: the FT of the entire data set expanded around f_5. Bottom panel: the residual FT after prewhitening with f_5 = 7289.0μHz. 59

Figure 4.8 Top panel: the residual FT after the first five modes have been removed from the data. Middle panel: the temporal spectrum after f_6 = 6632.8μHz and f_8 = 6631.9μHz have been removed. Note the change in amplitude scale. Bottom panel: the FT prewhitened by the f_9 = 6542.9μHz. 60

Figure 4.9 The FT of the entire data set at the low frequency end of the main power (top), followed by the residual FT prewhitened with the f_8 (bottom). 61

Figure 4.10 The original FT (top) followed by the residual FT (bottom) after the removal of the nine modes (f_1 to f_9). Note that the red (lower) solid line corresponds to $3\sigma_{noise}$, while the blue (upper) solid line corresponds to $3.7\sigma_{noise}$. The amplitude scales are different. 62

Figure 4.11 FT near f_{10} prewhitened by the nine frequencies, f_1 to f_9 (top) followed by residual FT after removing the tenth frequency f_{10} (bottom). 63

Figure 4.12 Total FT of the original WET data set on PG0014(top) followed by the residual FT of the same data set, prewhitened by the ten frequencies listed in Table 4.1. Note that the red (lower) solid line corresponds to $3\sigma_{noise}$, while the blue(upper) solid line corresponds to $3.7\sigma_{noise}$. The white solid line is σ_{noise}. 64

Figure 5.1 The ampitudes of the two best resolved modes f_1 on the top and f_2 is the bottom one (in red) for each individual run. 67

Figure 5.2 The phases of the two best resolved modes f_1 on the top and f_2 is the bottom one (in red) for each individual run. 68

Figure 5.3 The ampitudes of the two best resolved modes f_1 on the top and f_2 is the bottom one (in red) for subsets of data. 69

Figure 5.4 The phases of the two best resolved modes f_1 on the top and f_2 is the bottom one (in red) for the subsets of data. 70

Figure 5.5 Two statistical tests for the significance of the equal frequency spacing model with δ=66.7 μHz for PG0014+067. The top shows the KS test, the bottom the IV test. Values of -10 for the Q parameter are better than any values seen in prior asteroseismological studies of compact stars. 75

Figure 5.6 The same two statistical tests for the significance of the equal frequency spacing model with δ=90.38 μHz for PG0014+067. The top shows the KS test, the bottom the 2-D IV test. 77

ACKNOWLEDGEMENTS

I would like to take this opportunity to express my thanks to those who helped me with various aspects of my graduate student life that finally evolved into this thesis.

First and foremost, Steven D. Kawaler for his support, patience and guidance throughout my research and the writing of this thesis. Thank you for opening the door of science for me, for being a great teacher, researcher and friend, for letting me struggle but never let me fall.

Mike Reed for introducing me to Mr. Telescope and sdB stars and Reed Riddle for always being there to help with all the computer problems and issues I had.

Dave Oesper for being a devoted observing companion and Daryl for dispercing the clouds for me whenever the sky was closed.

My mother, father, sister and niece for all the love and strength they gave me.

And finally, this work would have not been possible if I did not have you, my dear friends. Thank you for being and staying beside me.

I would also like to thank my committee members for their efforts and contributions to this work.

ABSTRACT

One of the remaining mysteries of the stars like our Sun is what happens to them after their degenerate helium core ignites. Stars that represent this phase include the so-called subdwarf B (sdB) stars. The recent discovery that some of them pulsate (Kilkenny et al. 1997) opens a window to probe their interiors via astreroseismology. One of the most promising pulsating sdB (sdBV) stars for seismic analysis is PG0014+067. Brassard et al. (2001) reported 16 frequencies in the temporal spectrum of this star. As the authors show in their discovery paper this star indeed has very rich spectrum, too rich to be explained only with low order, low degree radial and nonradial p-modes. Therefore, they propose high ℓ modes to explain all the frequencies observed. A more recent suggestion by Kawaler & Hostler (2005) invokes evolutionary models of sdB stars which have rapid internal rotation. With these models, the rich mode density results from the presence of a few triplet (ℓ=1), quintuplet (ℓ=2) and radial (ℓ=0) modes.

As a tool to explore the question of possible rotationally split modes by a rapidly rotating cores in sdB stars, PG 0014+067 stands out as an excellent candidate because of the richness of its observed spectrum. To do so we need to determine, unambiguously, the oscillation frequencies present in the star. That is possible only with better frequency resolution and denser longitude coverage. Therefore, we observed this star with the Whole Earth Telescope for two weeks in October 2004. In this thesis I report the results of this multisite campaign. I find that PG0014+067 does not fit any theoretical model currently available.

CHAPTER 1. The last frontier of evolutionary models of an ordinary star: exploring the consequences of the helium core flash

Even though stellar evolution is one of the most mature areas in theoretical astrophysics, there are still phases in the life on an ordinary star (like our Sun) that are not well understood. We have a good grasp of how the stars form, and how they live for most of their lifetime while burning hydrogen in their core as main sequence stars. Also, we know how are they going to end their lives, slowly fading as white dwarfs. While there are still a few missing details, the story is fairly complete.

This narrative is a result of an elegant blend of observational and theoretical efforts in the past century. We would have a continuous evolutionary path of a low massive star all the way from its birthplace, a protostellar cloud, to its graveyard if it wasn't for one major gap: the core helium flash that initiates helium core burning. Unlike the most phases of stellar evolution, the flash itself occurs in a matter of minutes rather than millions of years. It is essentially a massive nuclear explosion in the center of the star releasing a vast amount of energy but only for a few minutes. Even though this huge amount of energy is released on a very short time scales, this apparently doesn't make the star explode, because we *do* see stars that are clearly survivors of this process.

By "looking" at the interiors of these survivors we can learn how the stars manage to survive this event of unstable helium ignition and plug this gap in the story of stellar evolution.

In this thesis I report on an observational effort to provide for asteroseismological analysis of a post helium core flash star, PG0014+067. One master's thesis won't solve all the missing puzzles however, our attempt is to answer some of the questions raised.

This chapter continues with the evolutionary problem at hand, giving a brief overview of the stellar evolution introducing the targeted group of stars. Chapter 2 explains the basic tools and methods needed to tackle this problem. The observations are presented in Chapter 3, focusing on the last Whole Earth Telescope campaign on PG0014+067. Chapter 4 analyses all the data gathered. Chapter 5 discusses the results of the data analysis and summarizes the findings.

1.1 Life of an ordinary star: the art of change

As stars evolve along the main sequence, they slowly turn the hydrogen within their cores to helium via nuclear fusion. When a star exhausts all of the hydrogen in the core, nuclear fusion ceases, and the core shrinks. The temperature in the layers above the core rise, and hydrogen starts burning in a shell around the core. The outer layers of the star expand, turning the star into a red giant. The helium ashes now generated from the shell settle onto the core, making the central mass of helium larger. The star begins to move up the red giant branch (RGB). From this stage in a life of a star, it will experience quite different evolution depending on its mass. This "crossroads" happens at the masses near 2.2-2.3 $M_{\odot}$.

1.1.1 Quiet helium ignition and beyond

For stars with masses that exceed 2.2-2.3 $M_{\odot}$ as the core gets more massive and continues to shrink, the helium becomes hot enough for helium fusion into carbon and oxygen. The star settles down to a new stable phase of core helium burning surrounded by a hydrogen burning shell. Once again, there is a nice thermostat to regulate the

internal properties. At this point, the star contains a helium fusing core and hydrogen fusing shell, surrounded by a very extended outer envelope, mostly made of hydrogen.

Given the poorer energy yield of helium burning and higher luminosity, a star's life on this helium 'main sequence' (HeMS) is much shorter than on the main sequence (MS). For example, a typical 1 $M_{\odot}$ star spends 10^{10} years burning hydrogen, i.e. on the MS, whereas it only takes 10^{8} years to exhaust the core helium. As the helium fuses into carbon (C) and oxygen (O) in the core, the C/O slowly accumulates at the center of the star. Eventually, the helium fusion is restricted to a shell outside a central core of inert carbon and oxygen (Hansen et al. 2004).

This phase is called the helium shell burning phase. During this phase of helium shell burning, the star again increases its radius, moving up and to the right (as the core contracts and the envelope expands), along the so-called asymptotic giant branch (AGB). The AGB star contains an inert carbon and oxygen core surrounded by the helium fusing shell, with the hydrogen burning shell on the top of it and the largely extended outer hydrogen (mostly) envelope. As the hydrogen burning shell dumps the helium ashes onto the helium shell this latter one builds up with time and undergoes an unstable phase called a thermal pulse. This in turn increases the mass of the carbon/oxygen core which makes the star bigger and more luminous. As the star climbs the AGB a wind develops in the star's envelope which blows the outer layers into space. The stellar wind causes a mass loss for an AGB star. This mass loss eventually reaches about $10^{-4}M_{\odot}$ per year (at the end), which means that in 10000 years the typical star will dissolve, leaving the central, hot dense core surrounded by a planetary nebula.

After it has exhausted the helium in its inner shell, a star has no way to generate more energy as there is no more hydrogen nor helium in its hot, dense central regions. When the pressure of radiation stops flowing outwards, the remaining outer layers of the star fall back inwards. The star shrinks upon itself, becoming denser. As the star becomes denser the pressure increases until the collisions between electrons in its core

provide enough pressure to halt the collapse. The star settles down into a final state of equilibrium as a white dwarf: a very, very dense body ($\rho \approx 10^6 g/cm^3$), with the mass of a star but the radius of a planet. The mass loss leaves behind a star with about 0.6 $M_\odot$. White dwarfs start out very hot, as a result of the high temperatures of their inner regions. It takes a long time for the heat to leak out to the surface and radiate away into space. Because they are so small, white dwarfs emit very little energy, despite their high temperatures. Their high temperature combined with their very small radius allows them eventually to settle at the lower-left corner of the HR diagram.

1.1.2 The Helium core flash and beyond

For stars with masses below 2.2-2.3 $M_\odot$, the evolution following the RGB is not so gentle. While on the RGB as the core gets more massive and continues to shrink, the helium becomes degenerate. The gas no longer behaves like an ideal gas, and the pressure and temperature become independent of one another. In this degenerate state the helium burning becomes unstable, with critical consequences resulting in the helium core flash. The moment at which the inner core begins to fuse helium to carbon is called the helium flash. This is a very sudden event in a life of a star, it happens on a timescales of the order of a minute. This is basically a runaway nuclear event near the center of the star releasing a huge amount of energy; the thermostatic control does not exist in degenerate matter. However, while computations of this process suggest an explosion, real stars somehow survive.

What happens afterwards, somehow, is that the temperature gradient of the star becomes very steep, to the point where most of the star outside the core becomes convective. The luminosity drops to about 100 times the luminosity of the Sun, and the star settles down into a quiescent phase of helium burning on the horizontal branch (HB). The star is in equilibrium again, stably burning helium in its core and fusing hydrogen in a shell surrounding it. This is illustrated in the Figure 1.1, where the evolutionary

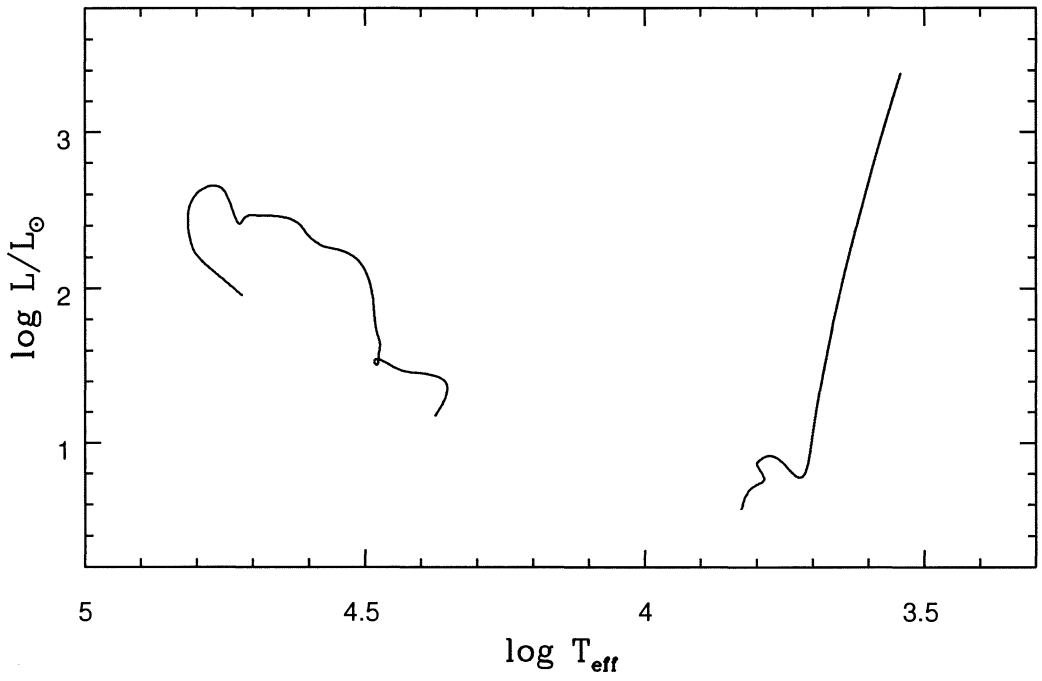

Figure 1.1 HR diagram with the evolutionary path of a $1.5M_{\odot}$, with the mass of the remnant (after the gap) of $0.48M_{\odot}$.

track of a 1.5 solar mass star is presented from the main sequence to the *RGB* and continuing from the zero age *EHB* (*ZAEHB*) as a 0.48 $M_{\odot}$ helium core burning star all the way to the white dwarf stage.

One interesting point about the helium flash is that the highest temperature during the flash is not in the very center of the star, but is instead in a shell at a radius containing about three tenths of a solar mass. Neutrinos serve to carry energy away from the star without generating thermal energy. Neutrino generation peaks in the very center, and decreases outwards. Thus the neutrino cooling is the most efficient in the very center, resulting in a lower temperature.

Following recovery from the flash, helium burning continues further in a similar way as it does in the higher mass stars, with a shell of hydrogen burning providing additional energy at the core-envelope interface. From the location of low mass helium core burning

stars in the H-R diagram, we know that some mass must be lost by the star to explain the distribution of the stars with $T_{\rm eff}$. This mass loss most likely occurs at the moment of the core flash in response to the runaway ignition and rapid reconfiguration of the core, but could occur along the RGB. This post-helium flash star resides on the so-called Horizontal Branch (HB) of the H-R diagram. Where the star will reside during its helium core burning on the HB depends on the mass of the hydrogen envelope that is left above the helium core. The smaller the envelope, the higher the surface temperature and the farther to the left the star will settle on the HB. Consequently, stars with no hydrogen left at all will end up at the far left of the HB.

Stars of low and intermediate masses evolve toward the white dwarf cooling sequence either through the post-AGB/planetary nebula or through the AGB-manqué/hot subdwarfs phases. On the way they cross various instability regions, i.e. variable planetary nebula nuclei, GW Vir stars (pulsating PG1159 stars) and/or variable hot subdwarf B stars.

1.2 Subdwarf B stars

1.2.1 General properties of subdwarf B stars

First studied in detail by Greenstein & Sargent (1974) the so-called 'hot subdwarfs' lie at the extreme hot end of the post helium-core flash sequence. Hot subdwarf stars are the Galactic field equivalent of the extreme (or "extended") horizontal branch (EHB) seen in some globular clusters, and they are the primary contributors to the ultraviolet excess observed in old stellar populations. Subdwarf B (sdB) stars are found to be the dominant population at all magnitudes comprising almost half of the objects brighter than 16th magnitude found in Palomar-Green survey of stellar objects with ultraviolet excess. According to evolutionary calculations by Dorman et al. (1993) sdB stars are burning helium in their cores while residing on the EHB. Their masses lie in a narrow

range $0.4 - 0.43 \geq M_\star/M_\odot \geq 0.52$. The lower limit is uncertain, as it depends on the minimum mass required to ignite helium. The upper limit is set by the the mass above which models evolve toward the AGB. These stars are the survivors of the core helium flash, and have convectively burning helium core. They have very thin, inert hydrogen envelopes with $q = \frac{M_H}{M_\star} \sim 0.0004$ which places them on the hot end of the horizontal branch (HB), so-called extreme horizontal branch (EHB).

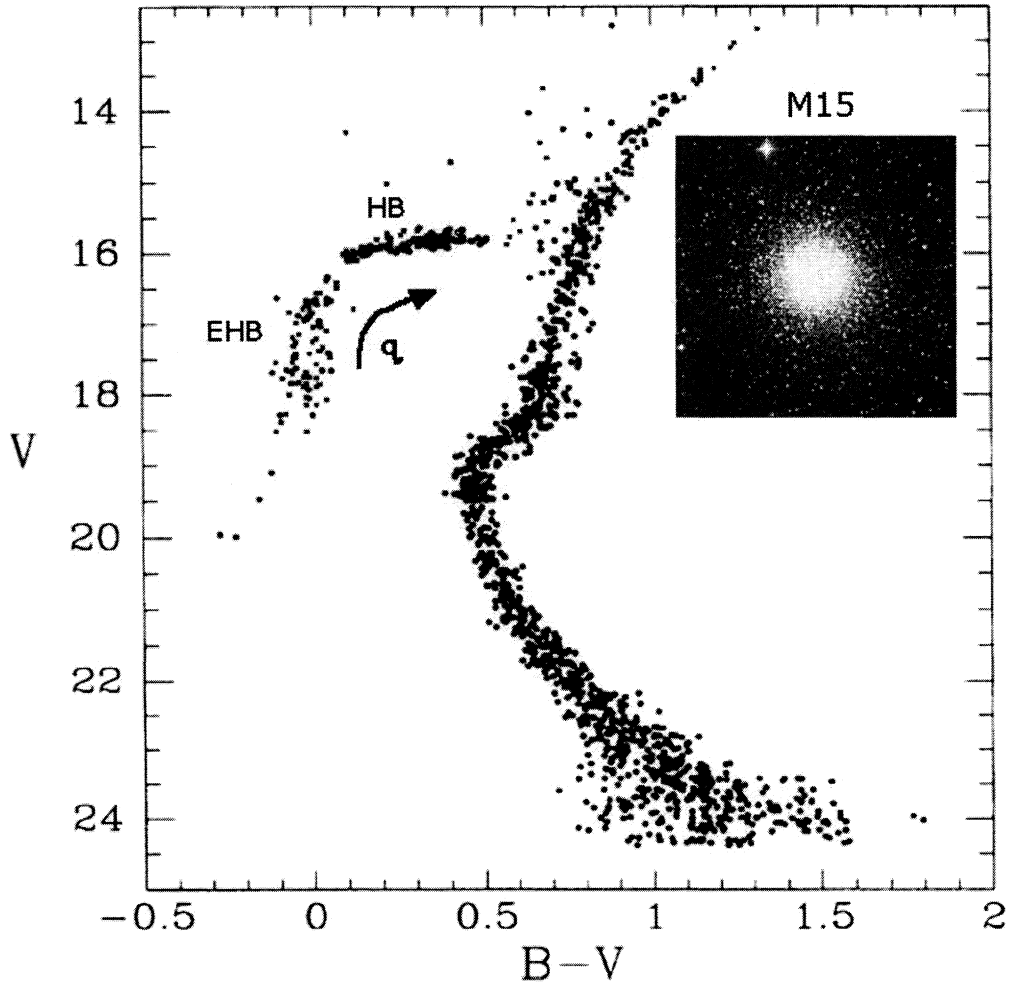

Figure 1.2 HR diagram of a globular cluster M15, pin-pointing the HB and EHB stages of the evolution. The insert shows the optical image of M15.

The whole evolutionary path of a low mass Population II star can be seen in Figure

1.2 where the color-diagram of a globular cluster M15 is plotted, together with the insert showing the optical image of the same cluster. Most stars are still on the main sequence, while some stars have turned off the main sequence toward the *RGB* (to the right and top). Stars that are burning helium in their cores are marked as *HB*. The hot tail (toward the blue) of the horizontal branch, where the sdB stars reside, is marked as *EHB*. Also, the dependence of the fractional mass of the hydrogen envelope (parameter q) on the temperature (or color) is shown.

The hydrogen burning shell is completely suppressed during HB evolution but becomes a significant energy source after core exhaustion. This fact distinguishes these stars from *EHB* models. Unlike the typical post-HB evolution, these objects do not ascend the asymptotic horizontal branch (*AGB*) after core helium exhaustion, since hydrogen is not burned continuously in a shell due to the very low envelope mass that cannot sustain hydrogen burning shell. Instead, they evolve directly toward the WD cooling track, and hence the name AGB-manqué [1] stars (Dorman et al. 1993). The fact that sdB stars have lost almost all of their hydrogen, but not all of it, makes them so enigmatic from the stellar evolution point of view. To lose that much mass, they have to suffer considerable mass loss during the *RGB* and most probably during the helium core flash.

The origin of the sdB stars is largely unknown. There are currently many competing theories for their origin which involve several possible channels. Single star evolution with an extreme mass loss on the *RGB* (e.g. D'Cruz et al. 1996) is one possibility. Different binary interactions such as common envelope binary evolution (e.g. Mengel et al. 1976), stable Roche lobe overflow (Han et al. 2002, 2003 and references therein), or merger of two helium white dwarfs (Iben 1990) or combinations thereof remain viable alternatives.

After more than a decade from the first quantitative estimate of the contribution

[1] Literal translation would be 'failed AGB' stars.

of different binary channels to the population of sdB stars was made by Tutukov & Yungelson (1990) it became clear from the observations of Maxted et al. (2004), that close binary evolution is indeed of great importance to sdB formation process: they find that two thirds of their sample of sdB stars are spectroscopic binaries with orbital periods of hours or days.

The most fundamental missing piece to our understanding of the evolution of the sdB stars is the nature and physics behind their mass loss (Fusi-Pecci & Renzini 1976). In order to end up this far left on the EHB they must lose nearly all of their hydrogen at almost exactly the same phase as the helium core has attained the minumum mass required for the helium flash to occur. As it has been shown by Vink (2004) the mass loss rates on the HB computed from radiative line-driven wind models are not high enough to create sdB stars. Their results show that HB winds are too weak to directly influence stellar evolution, and cannot create sdB stars as the sole effect. However, the puzzling chemical abundance patterns found in both field and cluster EHB stars are interpreted as due to the competing effects of gravitational settling and radiative levitation in the presence of a stellar wind. This is one of the gaps in stellar evolution picture that we hope will be filled in soon.

According to recent measurements of atmospheric parameters for sdB stars by Saffer et al. (1994), Maxted et al. (2001), Edelmann et al. (2003) and Lisker et al. (2005) effective temperature and surface gravity of the observed sdBs mostly lie within the theoretically determined start and end points for core helium burning on EHB, namely zero-age EHB ($ZAEHB$) and terminal-age EHB ($TAEHB$). This band lies along the convergence of evolutionary tracks shown on Figure 1.4.

It should be noted here that PG-like surveys find these blue stars easily because of their unique colors - thus even if quite rare, they are easy to find. On the other hand, these surveys might be showing us somewhat biased picture as there is probably a huge number of sdB stars that might be missing from the observational surveys due to

selection effects. These are primarily caused by main sequence companions that outshine the sdBs (main sequence type A and earlier) or appear as composite spectrum objects (main sequence type F to K).

1.2.2 Pulsating sdB stars

Observations of the HB stars revealed that some of these stars pulsate, letting us use the tools and techniques of asteroseismology to probe their interiors. Figure 1.3 presents the instability strips across the HR diagram, with the horizontal branch presented as the dotted-solid line. There are are two types of pulsating stars crossing this region of the H-R diagram: RR Lyrae variables and pulsating sdB stars, which occupy a high temperature 'tail' of the HB distribution, aka EHB.

1.2.2.1 EC14026 stars

The fact that some sdB stars pulsate was serendipitously discovered only a decade ago by the SAAO observers during the Edinburgh-Cape (EC) survey searching for blue stellar objects (Kilkenny et al. 1997). Commonly called EC14026 stars[2], after the prototype EC14026–2647, they are short period, low amplitude multimode pulsators. Typical periods are about 100-250s with the total period range of 80-600s. The pulsation amplitudes are generally less than a few hundredths of a magnitude.

Independently, their existence was theoretically anticipated by Charpinet et al. (1997). Theoretical analysis by Charpinet et al. (1996-2002) shows that the opacity bump caused by iron in the thin envelope is responsible for driving the pulsations via the κ mechanism. The κ mecahnism, or radiation blocking, is a well known pulsation driving mechanism. For instability to occur, the opacity in the driving layers must increase during the compression phase, to block some of the outward radiation. During the later expansion

[2]EC 14026 stars, also called sdBV stars by analogy with the pulsating white dwarfs, are now officially called V361 Hya stars.

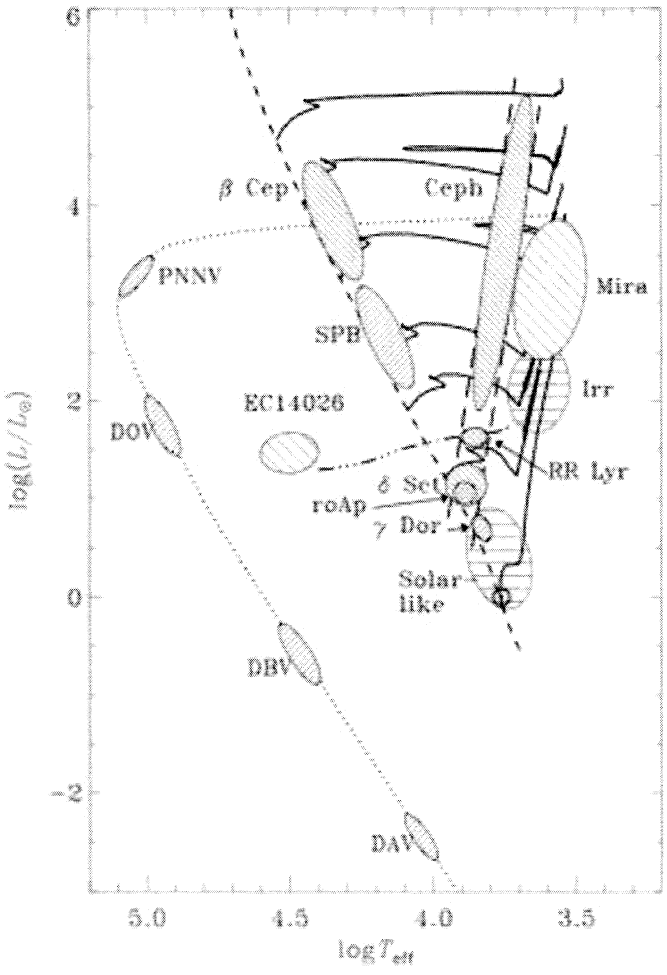

Figure 1.3 Schematic HR diagram illustrating the instability strips.

stage of the pulsation, this energy is then released with just enough delay to reinforce the expansion.

Following the discovery, additional sdBV stars were soon found mostly by teams at the SAAO (Kilkenny et al. 2002 and references therein), the University of Monteal (Billères et al. 2002) and the NOT (Østensen 2004) bringing the total of about 33 known EC14026 stars known to date.

The rapidly pulsating sdB stars occupy a narrow region in the $\log g - T_{\rm eff}$ space with the effective temperatures of $T_{\rm eff}$ = 29 000 - 36 000 K and surface gravities $\log g$ = 5.2 -

6.5.

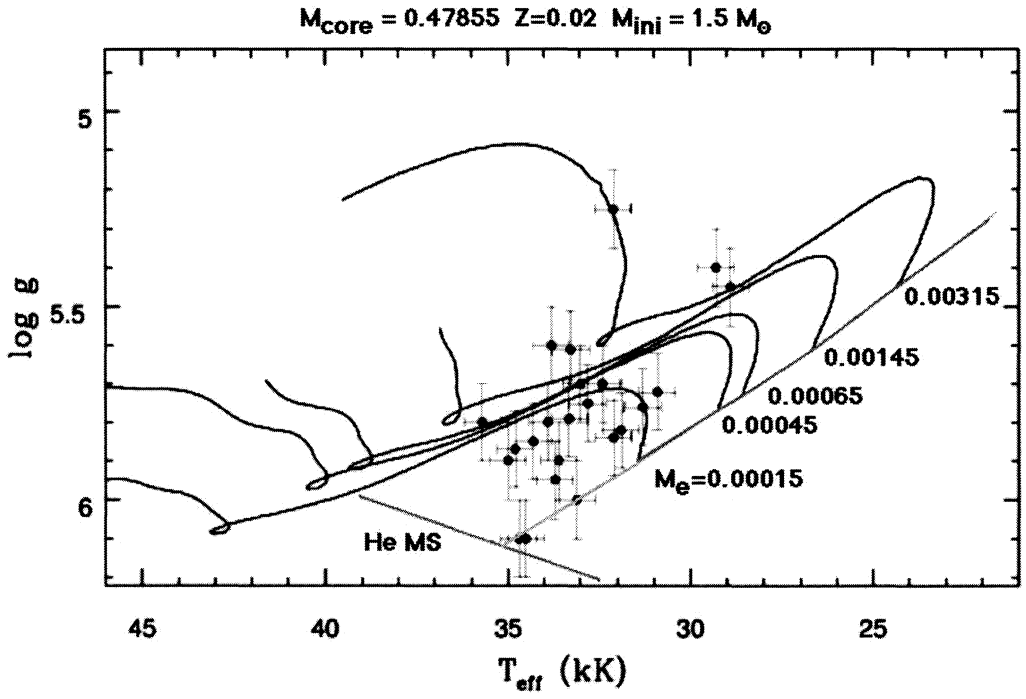

Figure 1.4 $\log g - T_{\rm eff}$ diagram with the observed sdBV stars. The theoretical evolutionary thacks are included (after Kawaler & Hostler 2005).

As it can be seen from the Figure 1.4 they tend to cluster around high surface gravities having a rather short periods in the range from 100 to 200 sec. Around 10 % of sdBV's have somewhat longer periods (300-500 seconds) and lower surface gravities (the representatives of this group are Feige 48 and PG1605+072).

When observed from a single site for a short interval, they usully show 2-3 dominant modes. A longer multisite campaign usually reveals more low-amplitude modes. For an review of the pulsating sdB stars see Kilkenny (2002).

It should be noted that not all stars in this region of the (log g - $T_{\rm eff}$) plane are pulsating. Why only some stars with similar atmospheric parameters pulsate is still an open question.

Spectrograms of the sdB pulsators reveal that most of the stars are composite in

nature comprising a hot subdwarf and a cooler main sequence F/G type star. The binary orbit should be derivable either from the radial velocity change (shorter orbital periods) or the light time effect (longer orbital periods).

Because the periods of pulsations of EC14026 stars are of the order of, and shorter, than radial fundamental, these pulsation are attributed to the low order and low degree pressure modes (p-modes).

1.2.2.2 "Betsy stars"

The new class of multimode sdB pulsators which oscillate on much longer timescales than their EC14026 counterparts, a factor of 10 longer, were discovered only two years ago by Elizabeth Green, and thus are commonly called "Betsy stars" or lpsdBV stars [3] (Green et al. 2003). The periods of this newly discovered class of stars range from 45 minutes to 2.5 hours. These rather long periods, greater than radial fundamental, imply that gravity modes (g-modes) are involved. The peak-to-peak amplitude variations in the light curves are comparable with those of most EC14026 stars ($\leq$ 0.05mag).

In addition to their very different timescales, these long-period sdB pulsators clearly populate a separate temperature and gravity regime than do short-period pulsators. They are found in the low temperature and low gravity domain of the $\log g - T_{\rm eff}$ plane where sdB stars reside. All long-period sdB pulsators with spectroscopially determined parameters are relatively cool ($T_{\rm eff} < 30,\,000$K) in contrast to the hotter EC14026 stars, and have surface gravities $5.4 < \log g < 5.7$. The strongest long-period variables show the characteristic beating effect of multiple modes with close periods. The fraction of sdB stars exhibiting long-period light variations is surprisingly high: roughly 75 % of sdB stars cooler than 30,000K, or 25-30 % of all sdB stars, in further contrast to the EC14026 stars which comprise less than 5 % of all sdB stars.

Fontaine et al. (2003) postulate that these stars are g-mode pulsators driven by the

[3]The "Betsy stars" are also called PG1716+426 stars after the prototype.

same κ mechanism that drives the pulsation in the EC14026 stars. The distribution of these stars in the $T_{\rm eff} - \log g$ plane suggests that their longer pulsations might be related to thicker hydrogen envelopes.

1.3 Goal of this work

Among the pulsating sdB stars PG0014+067 stands out as one of the richest pulsators. It was found to be a pulsating star by the Montréal group in their observations in June 1998 (Brassard et al. 2001). Aside from KPD1930+2752 (Poindexter et al. 2003) and PG1605+072 (Kilkenny et al., 1999) it shows the largest number of nonradial modes in the entire class, with at least sixteen present in the discovery paper. This star is a low-amplitude multimode pulsator, with periods ranging from 80 to 170 seconds. It is therefore a 'typical' pulsating sdB star with effective temperature of $T_{\rm eff}$ = 33 310K and $\log g = 5.8$. The richness of its pulsation, however, makes it a star of vital interest to the study of pulsating sdB stars and, by extension, the entire hot horizontal branch phenomenon. The rich mode density PG0014+067 has poses a fundamental challenge to understanding the pulsations of these stars, as there are not enough radial and nonradial modes with low degree ℓ ($\ell < 3$) to account for all of them without rotational splitting. One proposed solution, by Brassard et al. (2001), requires invoking modes with high degree (ℓ = 3 and even 4). They calculated a seismic model for M=0.49 $\pm$ 0.02 $M_{\odot}$ assuming a degree for the oscillation modes as high as ℓ=3 and 4.

An alternate interpretation was recently proposed by Kawaler & Hostler (2005) who pointed out that rotational splittings of ℓ = 1 and ℓ = 2 modes can cause sufficient frequency peaks in the observed range provided that the stellar core rotates much faster than its surface.

The only published observations of PG0014+067 are data from Brassard et al. (2001), who have observed this star using the 3.6 meter Canada-France-Hawaii Tele-

scope (CFHT) during five consecutive nights in June 1998. These data indeed show that the oscillation spectrum is complex, but being single site data they suffer from severe one cycle per day aliases, making the frequency identification rather difficult. To fully exploit this star we need to determine, unambiguously, the oscillation frequencies present. This can be achieved only by extended longitude coverage to obtain a sufficient frequency resolution, and to resolve the real pulsations from the inevitable one cycle per day aliases. Therefore, PG0014+067 was selected as the primary target for a Whole Earth Telescope campaign, Xcov24, held in October 2004. We observed this star from eighteen sites for two weeks during the Xcov24.

The main goal of this work is to fully exploit the WET data gathered on PG0014+067 resulting in better frequency resolution and precision. Only then can we critically examine competing theoretical models for these stars with minimal concern for diurnal aliasing. The resulting frequency list alone should be sufficient to verify the hypothesis that high ℓ modes are present in this star and/or test the prediction of large rotational splittings caused by rapidly rotating core. In either case, the rich observed mode spectrum of this star, as has been observed with WET, provides valuable input into modeling the structure of this important class of evolved stars.

CHAPTER 2. Asteroseismology - methods and tools

Before introducing the tools and methods of an discipline one should better know what it means.

Etymology: the term *asteroseismology* comes from a combination of three words:

astero: from Greek aster meaning a star,

seismos: also from Greek meaning tremor,

logos : meaning reasoning or discourse. Hence, if we were to translate literally, asteroseismology[1] would be the study of stellar tremors or starquakes, just as geoseismology is the study of earthquakes.

Asteroseismology is the study of the internal structure of pulsating stars by interpretation of their frequency spectra. More precisely, asteroseismology is a study of normal modes of pulsations in stars that display large numbers of simultaneously excited modes. The idea of learning about a physical system through the study of its normal modes of oscillation is an old physics trick, but relatively young in astronomy, as the data of sufficient quality to apply this technique to stars became available only a few decades ago. The most outstanding example is our own Sun. The study of normal modes in Sun shares the same etymology -if we just replace the Greek word for a star with the *Helios* meaning the Sun we get *helioseismology*.

Different oscillation modes penetrate to different depths inside the star. Therefore, if we are able to observe these mode of pulsation they can teach us about the interiors of

[1]For a thorough discussion on the why we are not calling it simply astro-seismology see Gough (1996).

stars. These oscillations provide information about the otherwise unobservable interiors of stars in a manner similar to how seismologists study the interior of Earth through the use of earthquakes.

2.1 Terminology and Basic Physics

Pulsations in stars are usually characterized by the nature of the restoring force. The observed pulsations in the Sun are essentially sound waves, in which pressure provides the largest part of the restoring force. Therefore, these modes are called p-modes. On the other hand, in the pulsations seen in the white dwarfs, buoyancy is the dominant restoring force. These modes are called gravity or g-modes. In general, nonradial pulsations in stars are manifest as a finite number of modes that follow the pattern of spherical harmonics used in other branches of physics. This spectrum of available oscillations is characterized by the eigenfrequency $\nu_{n\ell m}$, corresponding to a spheroidal mode with quantum numbers n, ℓ and m. The radial order n generally gives the number of nodes in the radial direction. The quantum numbers ℓ and m refer to the spherical harmonic Y_ℓ^m of a degree ℓ (the number of nodes on the surface of the star), and the azimuthal number, m, gives the number of nodal lines passing the equator (see, for example, basic texts in stellar pulsations such as Cox 1980, Unno et al. 1990).

A separate class of modes, the toroidal modes, also may exist in a star, and represent a slow twisting of a system. These modes correspond to oscillations of zero frequency (in the inertial frame) in which the displacement is transverse and divergence-free. In the case of a rotating star toroidal modes have non-vanishing frequencies of the order of angular frequency of the rotation, Ω, which are known as r-modes. In these modes the centrifugal and Coriolis forces play a similar role that pressure and gravity play in spheroidal modes.

In the asymptotic limit of $n > \ell$, the pulsation frequencies of p-modes become almost

equally spaced:

$$\nu_{n,\ell} = \nu_0(n + \ell/2 + \epsilon) + \delta\nu \tag{2.1}$$

where ν_0 the *large spacing*, ϵ a small constant (Tassoul 1980, 1990) and $\delta\nu$, the *small spacing*, are parameters that depend on the structure of the star. The asymptotic frequency spacing, ν_0 is a measure of the sound crossing time of the star:

$$\nu_0 = (2\int_0^{R_*} \frac{dr}{c})^{-1} \propto \sqrt{G\bar{\rho}} = 1/\tau_{ff}, \tag{2.2}$$

where c is the local sound speed, R_* is the stellar radius, G is the gravitational constant, $\bar{\rho}$ is the mean density of the star and τ_{ff} is the free-fall time. The sound travel time is (by the means of Virial theorem) related to the star's mean density and radius. With the typical mass of sdB stars of 0.5 $M_\odot$, ν_0 reflects the radius of the star and scales as $R^{-3/2}$. For sdB stars the free fall time is of the order of 100-200 seconds. Without precise mode identification, in particular its degree ℓ, asymptotic theory allows the measured frequency spacing to be uncertain by the factor of two, depending on whether modes of alternating even and odd ℓ (producing modes separated by $\nu/2$ in frequency), or only modes of the same ℓ with consecutive values of n are present in the star.

The asymptotic regime for g-modes reveals that high n modes are equally spaced in period with increasing n (Smeyers & Tassoul 1987),

$$\Pi_{n,\ell} = \frac{\Pi_0}{\sqrt{\ell(\ell+1)}} \times (n + constant) \tag{2.3}$$

where Π_0 is a constant that depends on the structure of the star (Kawaler & Bradley, 1994). Deviations from the mean period spacing (Π_0) tell us about the thickness of the stratified surface layers (Kawaler 1986; Bradley, Winget & Wood, 1993; Kawaler & Bradley, 1994) in white dwarfs.

When the frequencies of oscillations are comparable to the characteristic frequency ($\nu \propto \nu_0$), equations 2.1 and 2.2 do not apply. As rapidly pulsating sdB stars have periods of the order τ_{ff} they are in the non-asymptotic regime, we believe.

The frequencies of modes of the same n and ℓ and different m states are degenerate for any spherically symmetric system such as a non-rotating star. Rotation, however, can remove this degeneracy in ℓ in a way that is analogous to the Zeeman splitting of energy states in atoms. Borrowing here the analogy from atomic physics: in the same way magnetic field breaks the degeneracy in ℓ splitting the observed spectral lines of an atom into $2\ell+1$ equally spaced levels, where the splitting is proportional to the strength of the applied magnetic field, rotation lifts the degeneracy in ℓ with the splitting that is proportional to the rotation rate of a star. There will be a total of $2\ell+1$ equally spaced peaks for a given ℓ in the power spectrum of a rotating star.

In the case of rotation as a solid body, the m dependence of the oscillation frequency can be written as:

$$\nu_{n\ell m} = \nu_{n\ell 0} + \frac{m}{\Pi_{rot}}(1 - C_{n\ell}) \tag{2.4}$$

where Π_{rot} is the rotation period of the star, and the quantity $C_{n\ell}$ is a function of the spatial structure of the oscillations within the star. For sdB stars this term is usually a few percent and therefore can be neglected compared to unity.

Thus, for a given value of n and ℓ, rotation can produce $2\ell+1$ peaks that are equally spaced in frequency in the Fourier transform. An $\ell = 1$ mode becomes a triplet, an $\ell = 2$ mode a quintuplet, an $\ell = 3$ mode a septuplet if modes with all values of m are present. By convention (IAU Commission 27), modes with $m < 0$ so called 'prograde' have decreased frequency while modes with $m > 0$ so called 'retrograde' have increased frequency. For a more complete description of rotational splitting see the fundamental texts of stellar pulsation (Cox 1980; Unno et al. 1989).

If a star undergoes differential rotation with radius, i.e. $\Omega = \Omega(r)$, then the rotational splitting is given by

$$\nu_{n\ell m} = \nu_{n\ell 0} + m \int_0^R \Omega(r) K_{n\ell}(r) dr \tag{2.5}$$

where $K_{n\ell}$ is the rotation kernel corresponding to a mode of order n and degree ℓ. Thus,

for a star that is undergoing differential rotation with radius, the observed rotational splitting for a mode of given n and ℓ is an average of $\Omega(r)$ weighted by the rotation kernel $K_{n\ell}$ which is, in turn, a function of the eigenfunctions for the (n, ℓ) mode (Kawaler et al. 1999).

Given the recent discovery of the magnetic fields in hot subdwarfs by O'Toole et al. (2005) it seems that magnetic field might also play a role in hot subdwarf stars. They detected, by measuring the circular polarization in the hydrogen Balmer lines and in helium lines in a sample of hot subdwarf stars, magnetic fields with a strength of 1-2 kG in sdB stars. As an order of magnitude estimate of the influence of magnetic fields, we can compare the magnetic pressure ($mB^2/8\pi$) to the photospheric gas pressure; the ratio for sdB stars with fields of 2×10^3 G is $\frac{2\times10^5}{4\times10^5} \propto 0.5$, so magnetic fields could be important in sdB stars. Therefore it remains to be seen whether all subdwarfs have such high fields as the ones detected by O'Toole et al. (2005), and if so whether the pulsation of sdB stars are affected by it as in the case of roAp stars (Bigot et al. 2000; Cunha & Gough 2000).

2.2 High speed photometry

Since 1960s, high speed astronomical photometry has developed into a technique that has applications ranging from terrestrial and planetary meteorology to nuclear reactions occurring on the surfaces of neutron stars. High speed photometric observations of stars have been developed to study rapidly evolving phenomena such as occultation by solar system objects or somewhat more leisurely phenomena like pulsations in white dwarfs.

Our target PG 0014+067 is a multimode sdBV star with closely spaced periods of the order of a few minutes. This sets not only the requirement of having a short integration times, so that we have many integrations per pulsation cycle, but also a rather long time series to fully resolve the closely spaced peaks. To meet the above

requirements, the observations were made with fast readout charged coupled devices (CCDs) and photoelectric photometers (PMTs) during a two-week period through the collaborative efforts of the Whole Earth Telescope (WET) network.

2.2.1 PMT detectors

The photoelectric photometer (PMT) integrates photon-counts over equal time intervals using photomultiplier tubes (which generally have quantum efficiency of about 20%). For a detailed description of the typical instrument see Kleinman et al. (1996). In this WET run, the only PMT-based instruments used were three-channel PMTs. The three-channel PMT has two channels for uninterrupted measurements of the target and comparison star and a third channel is devoted solely to sky observations. This has a two-fold benefit. First, it eliminates the need to interrupt the data acquiring sequence for the sky measurements, giving a better spectral window. Second, having a continuous and simultaneous measurements of the sky background around the object, we are able to fully subtract the sky's contribution in the data channel. Three-channel photometers are excellent in recovering the clouds passing over by dividing the sky-subtracted variable with the comparison star. As an example how we can recover the data during cloud passage and in the case of some weird sky variations, see the discussion in Section 2.4.1.

2.2.2 2-dimensional Charge Coupled Devices: CCD detectors

CCDs combine high quantum efficiency (QE) with the ability to measure the target, surrounding sky and several comparison stars simultaneously. High QE (up to 90%) means that fainter stars can be observed with the same telescope. Simultaneous measurement of target, comparison stars and the sky background means that differential photometry can be obtained even under non-photometric conditions. Placing the aperture on the target afterwards, as part of the reduction process, rather that during the actual observations is a real advantage over photoelectric photometers.

All of the above means that CCD photometry is possible over a more extended range of conditions than was previously possible with PMTs. CCD photometers are superior than PMTs in many ways, but they tend to be relatively slow; most are designed for long integration times. The "dead" time, caused by slow readout electronics, between successive exposures can be very long (of the order of 10-20 seconds) and therefore troublesome for high speed-photometry of rapidly pulsating stars.

2.3 Photometric Issues

2.3.1 Noise

Atmospheric scintillation, transparency variations, and photon noise, usually define the limits of accuracy in photometry on timescales of less than a minute. Scintillation is caused by atmospheric turbulence along the line of sight and can be expressed as (Young 1967):

$$\frac{\Delta I}{I} = S_0 D^{-2/3} X^{3/2} e^{-h/H_0} \Delta\nu^{1/2}, \tag{2.6}$$

where X is the airmass [$\approx sec(z)$] and H_0 is the atmosphere scale height (taken to be 8 km),h is the altitude, D is the diameter of the telescope in cm, and the $\Delta\nu$ is in Hz. The scintillation noise is independent of the wavelength for telescopes with D $\gg$ 0.1m and it affects stars independently of their brightness. Since $\frac{\Delta I}{I} \propto D^{-2/3}$, the scintillation noise will be the smallest for the biggest telescope. For the conditions of good seeing $S_0 = 0.09$, and for integration time of 10s (making $\Delta\nu = 0.05Hz$) on a 2.56m telescope at altitude of h=2 000 m and a typical $X = 1.3$ gives an rms error in magnitudes of

$$\Delta m = 1.086\frac{\Delta I}{I} = 0.7mmag. \tag{2.7}$$

This would be a huge uncertainty in magnitudes for the millimagnitude precision needed for our photometric measurements. But this is the scintillation noise level for each point in the light curve, i.e. per one integration. Since we are calculating a Fourier transform

of the whole run, the overall time that enters as an inverse square root in Equation 2.7 will make the scintillation noise much smaller. The distribution of the amplitudes in a scintillation lightcurve is non-gaussian, it is well approximated by log-normal functions, evolving with time (Warner 1988).

For high-speed photometry, transparency variations generally predominate over scintillation in the low frequency regime. Photon noise on the other hand is "white noise" that varies inversly with the square root of the number of photons detected. Furthermore, we have to account for the noise introduced by detectors we are using. The overall signal-to-noise ratio of a measurement made with a CCD is given by (Mortara & Fowler 1981) :

$$\frac{S}{N} = \frac{N_\star}{\sqrt{N_\star + n_{pix}(N_S + N_D + R^2)}}, \tag{2.8}$$

where the signal term $N_\star$ is the total number of photons collected from the object, and the noise terms involve n_{pix}, the number of pixels under consideration; N_S, the total number of photons per pixel from the background of sky; N_D, the total number of dark current electrons per pixel; and R^2, the total number of electrons per pixel resulting from the read noise. The read noise is not a Poisson noise source, but a shot noise and therefore it enters into the noise calculation not as the square root but as a value itself.

Table 2.1 lists the relevantcharacteristics of the CCD detectors used in Xcov24. Given the characteristics of the CCD detectors in used in this WET run (Table 2.1) our measurements are dominated by the photon noise from the source and from the sky background. In this case, Equation 2.8 becomes:

$$\frac{S}{N} = \frac{N_\star}{\sqrt{N_\star + n_{pix}N_S}}. \tag{2.9}$$

A 10 s cycle time at the NOT, for example, gives a noise level of 3 mma per integration. Thus, count statistics dominate scintillation noise in our photometry. This noise level improves as the square root of the number of integrations. As an order of

Table 2.1 Characteristics of the CCD detectors used in Xcov24 on PG0014+067.

Site	Read noise in e^-	Gain in e^-/ADU
NOT	5.4	0.765
BOAO	7	1.8
SARA	5	5
McDonald	8	2
Loiano	1.73	2.13
Lulin	4.45	2
KPNO	2	7

magnitude the signal-to-noise ratio of a 4h observation with a 2 meter class telescope on PG 0014+067 from the WET data is $\frac{S}{N} \approx 11750$, corresponding to $\Delta m \approx 0.1$ mma.

2.3.2 Aliases

When the Fourier transform of the data set is calculated, each coherent frequency present in the data appears as a peak, with the side-lobes and aliases due to the finite length of the data set and to gaps present. The spectral window illustrates these artifacts. The spectral window is calculated by constructing a data set with a single noise-free sinusoid sampled at exactly the same time and with the same intervals as the real data. Therefore, the spectral window will have the main peak at the input frequency of the sinusoid, but will show aliases and side-lobes introduced by the gaps in the data set and by the finiteness of the time domain. If the data set is composed of multiple frequencies, each peak will be accompanied by a corresponding spectral window. Therefore, not all peaks in the observed power spectrum correspond to the real frequencies in the star.

To illustrate this, consider two runs run taken from the same site separated in time by day. Figure 2.1. shows the power spectrum of the combined data set and its corresponding spectral window. The first panel shows the spectral window, where the central frequency corresponds to a sinusoid of the frequency $f = 6826 \mu Hz$. As we can clearly see, it is surrounded by two other peaks, equally spaced beside it, separated by

$\Delta f = 11.57 \mu Hz = 1/\text{day}$. These features are one cycle per day aliases. The second panel shows the power spectrum of the real data in the same frequency range. Not only that is hard to determine unambiguously which is the correct frequency, but in this case it is impossible – as we will see later. If we were to select naively at the highest peak among the forest of peaks in this FT, we would have chosen the one cycle per day alias of the true pulsation frequency of the star. This remains the biggest problem of single site observations, no matter how big the telescope we might have (or however good the signal-to-noise ratio is).

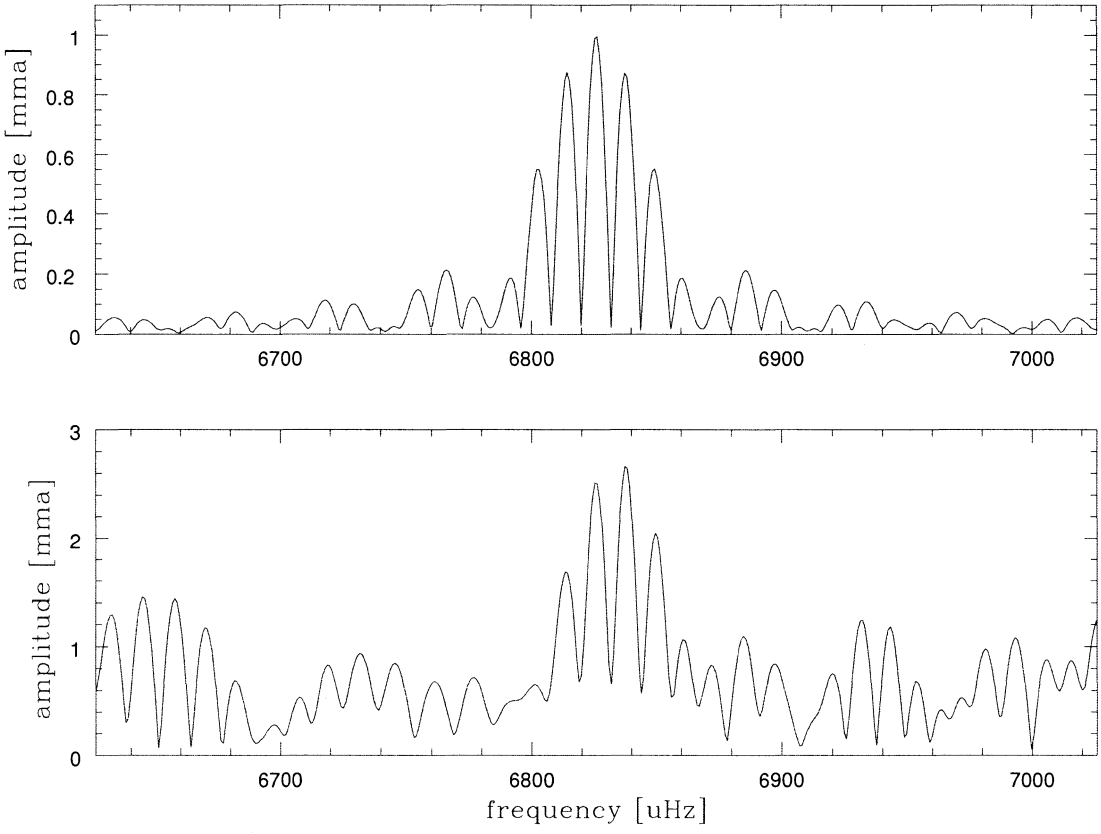

Figure 2.1 Two single site runs (lulin-0008 and lulin-0010 with the average length of $\approx$ 7 hours) on PG0014+067 taken in two consecutive days obtained during Xcov 24- centered near the main frequency. The first panel shows the spectral window.

When we have several runs irregularly spaced in time, we must calculate a spectral

window to visualize the aliases and side-lobes present. This situation is illustrated by Figure 2.2, where the spectral window of the real data is shown at the top. The FT of the light curve of seven combined runs from the Xcov 24 centered at two different frequency regimes, is presented in the lower two panels. The frequency of the central peak in the spectral window is chosen to be the same as in the previous example, $f = 6826\mu$ Hz and corresponds to a true periodicity in the star. As we can see, the spectral window can be very complicated, although one cycle per day aliases are somewhat reduced. If we superimpose this spectral window on the large peak in the FT of the second panel, we can in this case identify the peaks that are aliases and therefore not real frequencies of the pulsation. The situation becomes more complex when there are closely spaced frequencies, as it is the case in the frequency domain around 7090 μHz. The spectral window "masks" the true picture, and the Fourier transform of such irregularly spaced data possess features that can make unambiguous interpretation difficult or even impossible.

The only cure for a bad window is getting a better one. Therefore, the prescription for overcoming this problem is to observe as long as possible and as continuously as possible. Only with the spectral window that has the aliases significantly reduced and simplified can we expect to be able to unambiguously determine the real frequencies of stellar pulsations, which is the basis of any attempt to perform a meaningful asteroseismological study on a star.

2.4 Reduction Techniques

The goal of our time series analysis is to extract the frequencies of oscillation. To perform the frequency analysis we first have to 'prepare' the data for the analysis. The software used for the reduction is XQED (Riddle 2003). XQED, an evolved version of QED written by Ed Nather (Kleinman et al. 1996), is an Xwindows task designed to

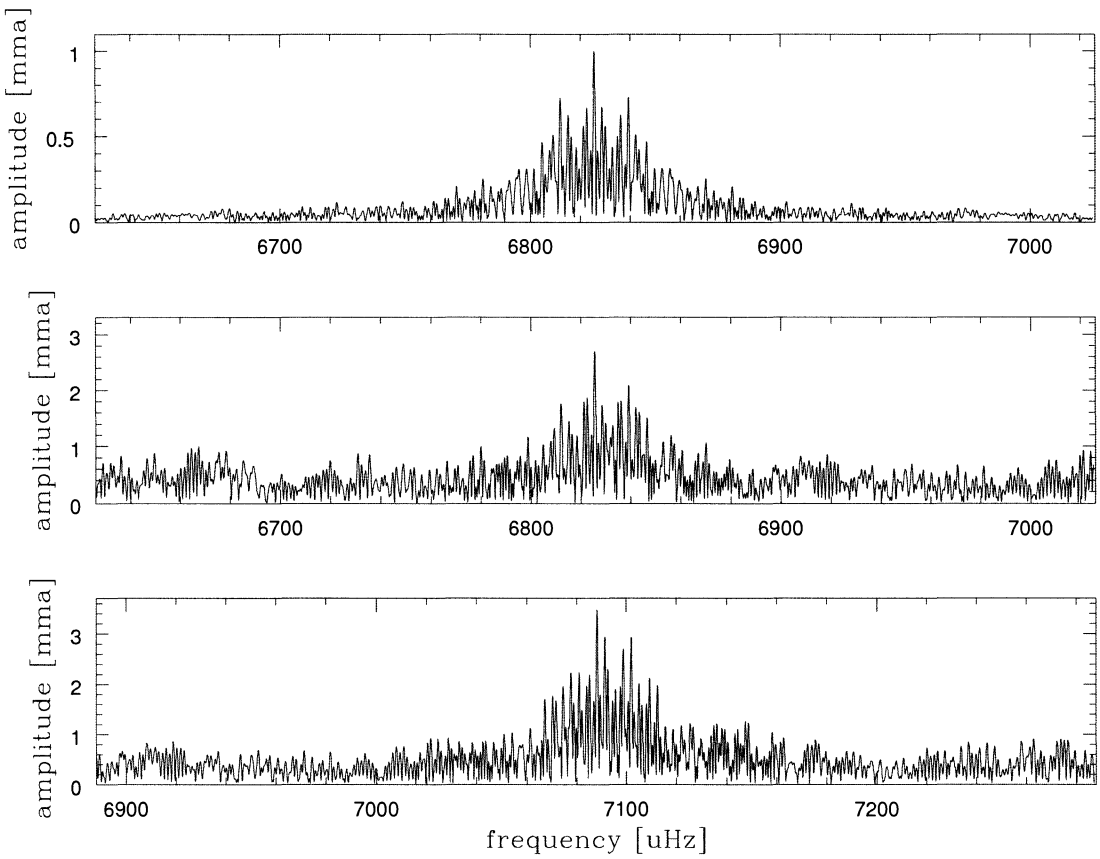

Figure 2.2 Seven runs on PG0014+067 taken during Xcov 24: sara213, sara214, lulin-0001, NOT-001, lulin-0008, lulin-0010 and maja10192004. Top panel shows the window.

reduce and analyze differential photometry data taken by both PMTs and CCDs.

2.4.1 Reduction of PMT data

In the three channel PMTs used in this WET run, the third channel was devoted to the sky background measurements. To account for the different sensitivities between the channels, the sky background was measured in all three channels at the beginning and at the end of each run. The raw data consist of photon counts for the target (channel one), a nearby comparison star (channel two) and a sky counts (channel three) observed

through small apertures [2] in the focal plane. After proper dead time correction, the sky background (channel three) was subtracted both from the target and from the comparison star point by point. The variable star data were then divided by the comparison star to remove transparency variations. To correct for any low-frequency variations caused by seeing and differential color extinction, the resulting light curve was then fitted with the low order (2-5) polynomial. Bad points, coming from either electronic noise, guiding errors or clouds, were removed by hand. Finally, the light curve was mean–subtracted leaving only the variations from the mean ($ma = \Delta I/I$) and a barycentric correction to the exposure mid-times was applied giving the times of the data points projected to the center of the solar system.

Figure 2.3 presents a typical PMT run on PG0014+067. These PMT data were taken in white light, at the 2.16m telescope of National Astronomical Observatories Chinese Academy of Sciences (NAOC). The exposure time was 5 seconds, the length of the run was 7.5 hours with a total of 5401 data points. In this figure, the panels show in order from the top to bottom: the light curve of the target star (this is the reduced light curve derived in the way explained above, with the polynomial of the third order), comparison star (this light curve is sky subtracted and fitted with the polynomial of the third order), and the sky. The next panels show the Fourier transform of the corresponding light curves in the same order. Note the jumps in the sky level (channel three). These apparent changes in the sky level were due to the presence of the construction lights at the observing site. Normally, any astronomical observations are made at the dark sites far away from any city or other lights interfering with the data, but life wouldn't be as interesting if there are no exceptions to the rules. The NAOC had construction going on because the building of the 4 meter telescope LAMOST took place at the time of our run. As they were behind schedule, they decided to work 24 hours/day, necessitating

[2]The aperture size is selected to minimize the light from the sky while collecting all the light from the target star and was varied depending on seeing conditions.

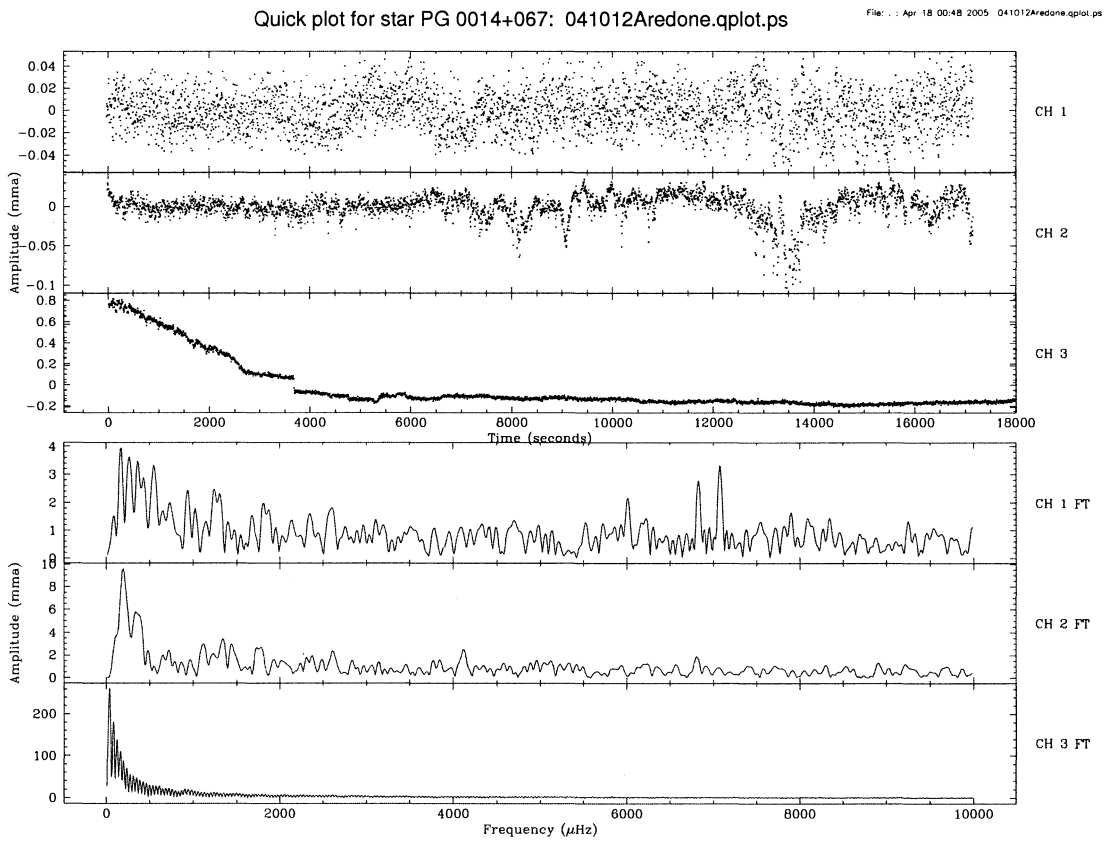

Figure 2.3 A sample of a PMT run on PG0014 obtained during Xcov 24

construction lights to be turned on during the night as well. By having the third channel continuously and simultaneously measuring the sky background we were able to recover much the data. Furthermore, note that the conditions were not perfectly photometric either, as there were some thin cirrus passing over the observed part of the sky (seen as dips in channel 2). Nontheless, the power spectrum of this, in many regards troublesome, run shows the two main peaks near 7 000μHz with a amplitude of 3 mmag.

2.4.2 Reduction of CCD data

The CCD measurements were acquired with a number of different cameras, each having different characteristics (see Table 2.1). To account for this diversity, each ob-

servation was followed by a standard set of calibration images: bias, dark and flat-field frames, as explained in Chapter 3.2.1. The observations were taken in 'windowed' mode, optimized to acquire at least two comparison stars in the same field as the target and minimizing the readout time, ensuring the highest duty cycle possible. In this way, consecutive data points were obtained in 5 to 25 s intervals, depending on the instrument.

The raw CCD data were reduced using IRAF[3] CCDPROC package. The reduction comprised correction for bias, dark counts and flat-field. Further photometric measurements (aperture photometry) on these reduced frames were made using the PHOT package. After carefully examining the extracted aperture photometry for a set of different apertures for each observation, the aperture that gave the best signal-to-noise ratio was used. The apertures that typically gave the optimal signal-to-noise ratio in the resulting light curve had a radius of $\approx$1.75 times the FWHM, with the surrounding annulus to determine the local sky level. In this way each star in the frame has its own corresponding sky channel.

The time-series measurements derived in this way were then imported into XQED (Riddle 2003), the photometry analysis software for the WET. The further analysis (differential photometry) was similar to the PMT data from now on, only now we had more than one comparison star. Each corresponding sky channel was subtracted from the target star and all the comparison stars. For each light curve, we performed a point-by-point division of the target star by the average of the best choice of comparison stars. We then corrected for any low-frequency variations, caused by differential colour extinction, by fitting and removing a low-order polynomial. Finally, the mean light level was subtracted and the barycentric correction to the exposures mid-times was applied. The resulting light curves, showing a fractional variation of the intensity of light as a function of time are presented in the Chapter 3.2.2, Figure 3.3.

[3]IRAF is the Image Reduction and Analysis Facility, a general purpose software system for the reduction and analysis of astronomical data provided by NOAO.

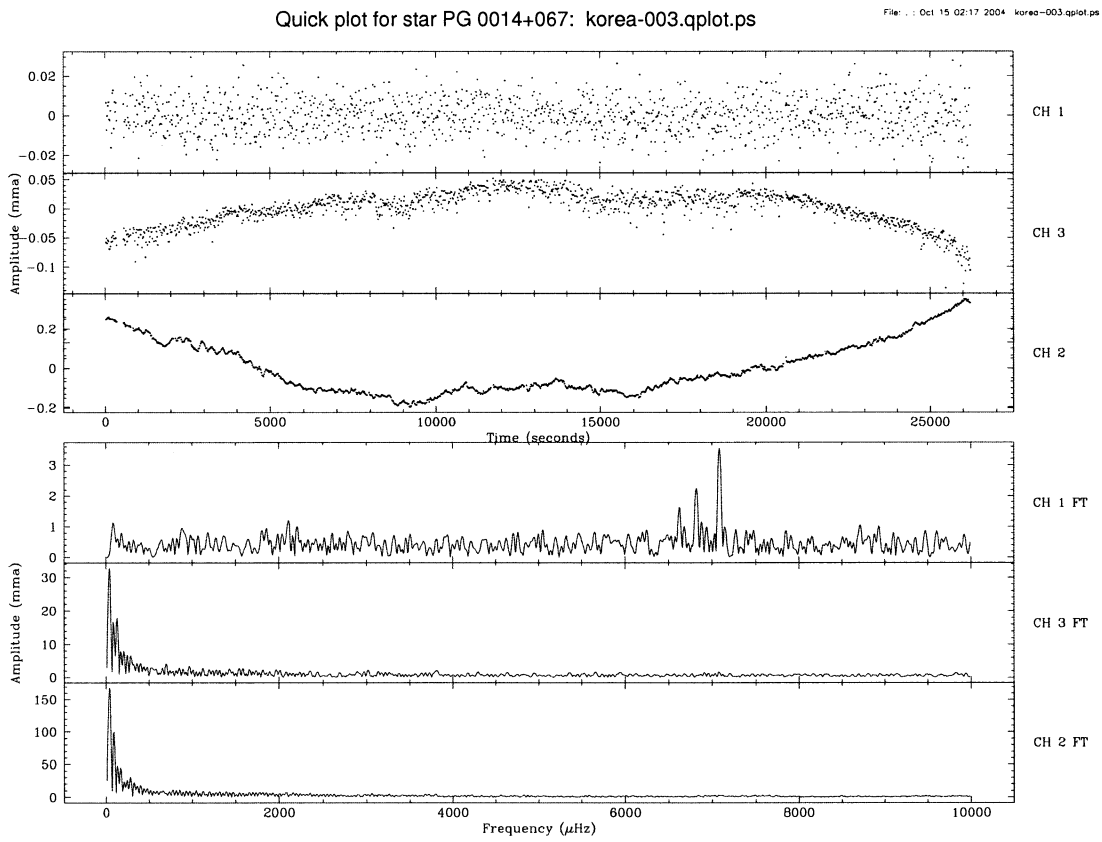

Figure 2.4 A sample of a CCD run on PG0014 obtained during Xcov 24.

The 'typical' CCD data from the BOAO 1.8m telescope are shown in Figure 2.4. The data were taken without a filter, with the cycle time of 20 seconds (actual exposure was 11 seconds). There were two comparison stars in the frame. The upper panel shows the actual light curves, starting with the variable star at the top, one comparison star in the middle and the sky at the bottom of the first panel. The second panel shows the Fourier transforms of the light curves in the same order as mentioned above. Even though this was a smaller telescope than the one used at NAOC with a lower duty cycle, the advantages of a CCD photometry are striking. The scatter in the light curve is much smaller, resulting in the cleaner power spectrum where the three highest peaks can be resolved, with the noise from the spectrum being < 1 mmag.

CHAPTER 3. Whole Earth Telescope observations of PG0014+067

The Whole Earth Telescope (hereafter WET) is a world-wide network of observers and researchers whose aim is to overcome the inevitable natural consequence of Earth's rotation -namely the bad spectral window. Chapter 2, Section 2.3.2, demonstrated the inadequacy of single site data for reliably determining the frequencies of stellar pulsation. The conclusion from that chapter was that the only way around this problem is to improve the spectral window. The WET network tries to accomplish this by coordinating telescopes around the world to observe the same object (or a few objects) nearly continuously from observing sites distributed in longitude. The number of independent sites participating in WET runs depends on the availability of the telescope time, from six sites in the very first run (1988) to about 20 sites in the recent years. Participating telescopes range in the aperture from 0.6 m to 3.6m. Because of significant organizational and scheduling issues the WET assembles itself only once or twice per year. The runs typically last for about two to three weeks, usually followed by a few scattered observations before and after the main campaign.

This chapter presents the results of the most recent WET run (Xcov24) with the subdwarf B star PG0014+067 as primary target. We present the latest WET run with the description of techniques we used, followed by the data reduction process specific to this star. The next chapter discusses the results of an in-depth analysis of PG0014+067 data gathered in Xcov24.

3.1 Telescope allocations and weather

All observations presented in this work result from the Whole Earth Telescope (WET) multisite time series photometry campaign (Xcov 24) held in October 2004. The main window of the WET campaign on PG 0014+067 (hereafter PG0014) was during October 7-21, 2004.The principal goal of our campaign on PG0014 was to obtain good longitude coverage over a 2-week time period to adequately resolve the Fourier transform at sufficient frequency resolution for asteroseismic analysis.

PG0014 is a faint star, with a B magnitude of 16.5, and a low amplitude pulsator - most modes have amplitudes below 2 mmag. Thus we generally needed larger that average ($\geq$2 meter) class telescopes distributed around the globe. This requirement was fulfilled; time was allocated to 5 bigger telescopes ($>$ 2m) that were nicely spread over the longitude so that, in theory, we could observe the star continuously given good weather conditions.

Together with the 13 smaller telescopes we had 18 sites participating in this campaign. Telescope time allocation and corresponding observatories are presented in Table 3.1. At an RA near 0h, and a near-equatorial declination of +7 degrees, PG0014 was equally accessible from both northern and southern hemisphere sites during this time of the year. As a contingency, smaller telescopes ($<$ 2 m) with CCD detectors were included to minimize the gaps in the data and simplify the alias pattern of our spectral window.

Even though we had good potential for dense time coverage with both bigger and smaller class telescopes for Xcov24, the weather was not cooperative. The non-photometric conditions all over the globe during the campaign resulted in quite sparse coverage. As an example, we had only one run (with poor photometric quality, because of hazy and cloudy conditions) out of ten nights at Pic Du Midi, one of the 2m telescope in the WET run. During the ten available nights this site had a range of weather from clouds,

Table 3.1 Participating sites in Xcov24.

Site	Location	Telescope(m)	Instrument	Time (Oct 2004 UT)
Tenerife	Spain	0.8	CCD	7-14
NOT	Spain	2.6	CCD	12-16
LNA	Brazil	1.6	CCD	11-20
Gemini South	Chile	8.1	CCD	queue-time
Mt.Cuba	Delaware, USA	0.6	CCD	8-22
McDonald	Texas, USA	2.1	CCD	15-16
KPNO	Arizona, USA	2.1	CCD	16-22
SARA	Arizona, USA	0.9	CCD	8-9, 11-16, 18-22
Mauna Kea	Hawaii, USA	0.6	CCD	12-21
Mt.John	New Zealand	1.0	CCD	10-14
BOAO	South Korea	1.8	CCD	12-19
Lulin Obs.	Taiwan	1.0	CCD	11-20
NAOC	China	2.16	PMT	12-18
Moletai	Lithuania	1.65	PMT	7-21
Mt.Suhora	Poland	0.6	PMT	8-22
Kolkony Obs.	Hungary	1.0	CCD	7-20
Vienna Obs.	Austria	0.8	CCD	3-10
Loiano	Italy	1.5	CCD	8-12
Pic Du Midi	France	2.0	PMT	9-18

fog and blizzards to snow. The weather conditions were not much better at other bigger telescope sites. The 2.56m Nordic Optical Telescope (NOT) at La Palma got two clear nights out of five, albeit with a very good conditions. The 2.1m telescope at Kitt Peak National Observatory (KPNO) got two clear nights out of the seven ones allocated. China had somewhat better weather, but they had considerable problems with the nearby construction during the actual observations; the construction lights were 'on' during the whole night which can indeed be seen in their light curve(see Chapter 2.4). The site in New Zealand, Mt. John Observatory, had bad luck in that during the only clear night the photometer malfunctioned; it was fixed promptly, but then the winds were so high that the observer could not even open the dome, when the winds calmed down the clouds continued the 'weather conspiracy game'. The 1.6m telescope in Brazil (LNA) had very bad weather too; they only got a 2 hour clear gap during a single

night out of ten. Unfortunately, no observations were acquired within Gemini South queue-time.

On the other hand, surprisingly good data were obtained by the SARA 0.9m telescope at KPNO. As can be noticed from the log of the observations given in Table 3.2, most of the data didn't come from our bigger telescopes (> 2m), but from moderate size ones (between 1m and 2m). Lulin Observatory in Taiwan, with their 1m telescope, gave an excellent data set of six runs, followed by the Bohyunsan Optical Astronomy Observatory (BOAO) 1.8m telescope in Korea. Despite the terrible weather and some unexpected instrumental problems, the 2 week core campaign resulted in a data set of about 180h of data on the primary target giving the duty cycle of about 58 %. This duty cycle falls within, although to the lower end, of the normally achieved coverage of 50-90 % by WET.

3.2 Observing Techniques

The telescopes used for the primary target range in aperture from 0.9m to 2.56m. Data from NAOC (China), Moletai Obs. (Lithuania) and Pic Du Midi (France) were obtained using three-channel PMTs as described in Chapter 2. Exposure times were 5 seconds for 2m telescopes (China and France) and 10 seconds for 1.65m telescope in Lithuania. Channel 1 measured the program star, channel 2 measured a local comparison star and the third channel simultaneously recorded sky background. No filters were used during any of the photometric observations to maximize the photon count rate.

All other data were obtained using CCDs. For the CCD measurements, exposures ranged from 5-15 seconds depending on the size of the telescope. As the readout times differ from chip to chip and were quite long for some sites, observations were made in the "windowed" mode, i.e. only the portion of the chip was read out to minimize the cycle time, making sure there were always at least two comparison stars in the frame. In

this way, consecutive data points were obtained in 5 to 25 s intervals, depending on the instrument. Data from McDonald and KPNO used BG_40 filters and data from NOT used a W#92 filter. The field of view was different for each site, as it depends on the focal length of the telescope and the size of the CCD chip.

Figure 3.1 shows the 15 x 15 arc minute field of view indicating the target star. This was an easily recognizable field due to the proximity of the bright galaxy, UGC 155, just to the west of PG0014. As was mentioned above, each CCD site used the windowed mode to reduce the read out time, so the actual CCD frames at every individual site were never bigger than 5 x 5 arc minutes centered around the target. The number of comparison stars depended on the size of this window, having from two to six comparison stars in the frame.

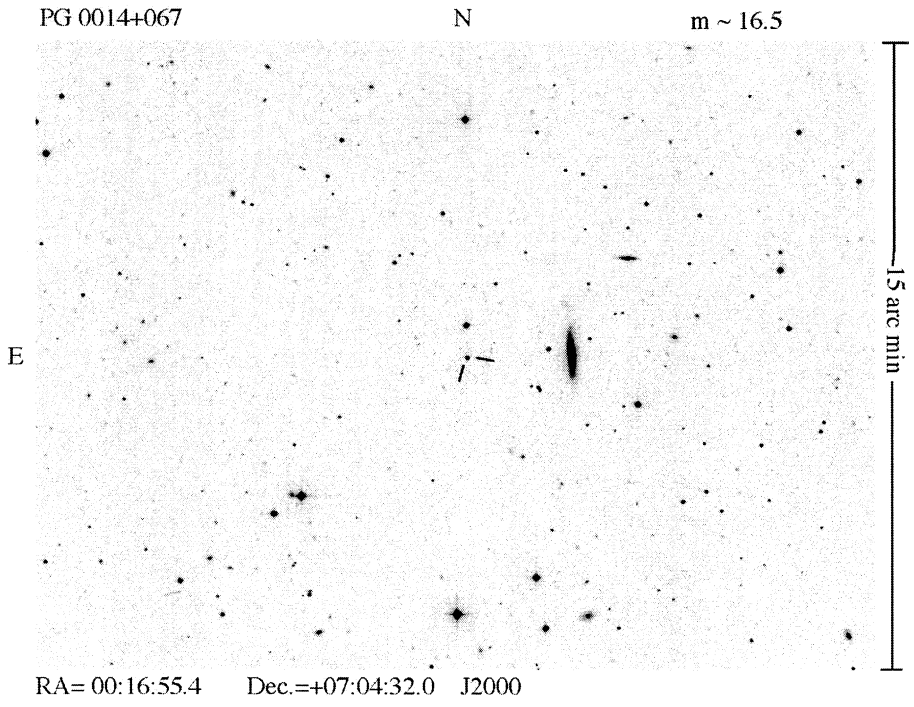

Figure 3.1 Finder chart for PG0014+067 together with all possible comparison stars used.

Together with the science frames, each night of observation included calibration images. Bias frames (at least ten zero length exposures with the shutter closed) were

taken at the beginning and end of each data run. These bias frames were used to correct for any bias pattern that particular chip might have. Dark frames (at least 10 frames with the shutter closed and the exposures as long as the integration time for the data frames) were taken in series at the beginning or end of each data run. These dark frames were used to correct for any hot or bad pixels and possible leackage of the light on to the chip. At least 10 flat field frames (sky or dome flat frames) were taken each night with exposures chosen so that the counts on the chip were about 50 % of the saturation level. The flats were used to correct for different pixel sensitivity and to remove any pixel to pixel variation along the optical path.

3.3 Data reduction

Preliminary, 'on the fly', data reduction was done during the campaign at headquarters (held in Ames at Iowa State University). Since the WET does not have a standard CCD photometry extraction package yet, raw CCD frames were pre-reduced (overscan, bias, dark, flat filed corrected) by the observers using their own software immediately after the run and sent to the headquarters (HQ) in the the standard WET/XQED format. During the WET run the incoming data were further reduced at HQ using the WET software XQED (Riddle 2003). The goal of the WET HQ is to do the fast data reduction allowing HQ staff to track the data gathering process in near-real time, and therefore to identify necessary changes in the observing strategies and problems thereof. HQ also posts the data to the website so that all the participating astronomers can see how they are doing.

The process of this preliminary data reduction was as described in Chapter 2, Section 2.4. As both the target and the comparison stars were in the same CCD frame, differential photometry removed the the extinction and sky variation. However, since the extinction is wavelength-dependent, color differences between the stars produced

small non-linear trends in the data. These trends were removed by dividing by a low order (2-5) polynomial fitted to the single night data. For the explanation of the detailed data reduction see the Section 2.4. The PMT data were reduced as described in Section 2.4.1; an example of the three channel PMT run is shown in Figure 2.1. The resulting individual light curves presenting the fractional variation from the mean together with its Fourier transform (FT) was then added to the total light curve and corresponding total FT.

The complete list of observations of PG0014 acquired during Xcov24 is given in Table 3.2. Although many hours of data on PG0014 were collected during Xcov24, the longest *continuous* coverage is unfortunately only nine hours, due to the rain, snow, blizzards and other 'prirodne nepogode' [1]. Figure 3.2. shows the main coverage of the Xcov24 data. All the light curves presented are the result of the data reduction process explained in Section 2.4.

To have a uniform data system the policy of the WET is that all the data are carefully re-reduced by one person after the actual campaign. The detailed re-reduction of all the data gathered during the Xcov24 on PG0014+067 used in this analysis was carried out by the author as part of this Thesis. We now move on to the detailed frequency analysis of the WET data in the next Chapter.

[1] Serbian phrase, literal translation would be 'foul of nature' or in slang 'foul weather'.

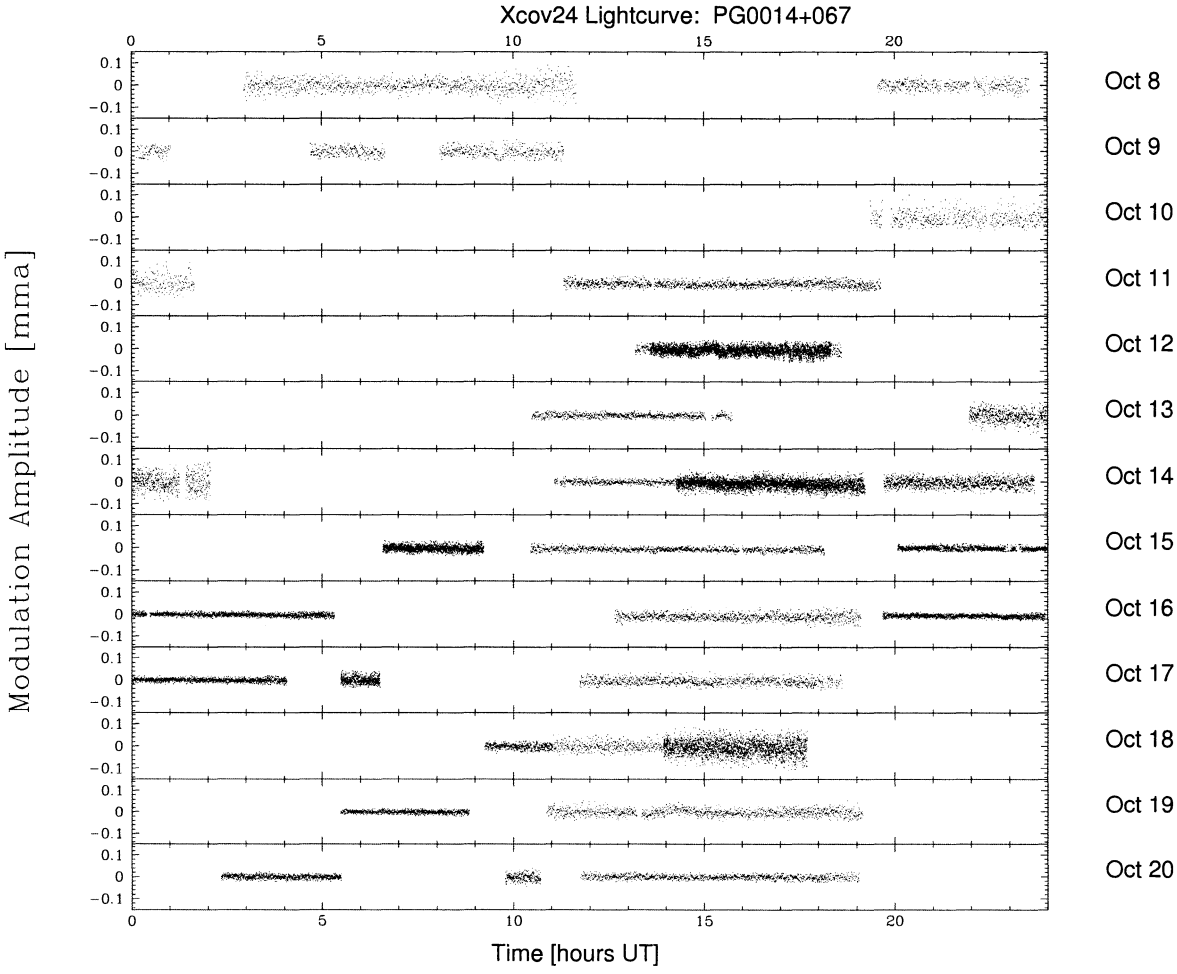

Figure 3.2 Light curve for data on PG0014 obtained during Xcov 24.

Table 3.2 Journal of observations : Xcov24 data on PG 0014. Runs marked with asterisks were not used in the final analysis due to the bad signal to noise ratio.

Run name	**Telescope** (m)	**Date** (Oct 2004 UT)	**Start time** (UT)	**Run length** (hours)
mdr275*	MDM1.3	05	08:55:15	2.10
teide-10072004*	Tenerife0.8	08	02:36:40	0.55
sara213	SARA0.9	08	02:47:59	8.74
PG0014_08oct04	Loiano1.5	08	19:24:50	5.50
sara214	SARA0.9	09	01:58:59	9.20
PG0014_09oct04*	Loiano1.5	09	19:45:09	1.44
PG0014_10oct04	Loiano1.5	10	19:09:20	6.35
lulin-0001	Lulin1.0	11	11:10:35	8.35
041012A	NAOC2.16	12	12:27:00	7.50 PMT
korea-001	BOAO1.8	12	13:02:10	5.45
korea-002	BOAO1.8	13	10:19:20	5.32
041013A*	NAOC2.16	13	11:27:22	8.50 PMT
lit-01	Moletai1.56	13	21:49:20	4.65 PMT
france-01*	Pic Du Midi2.0	13	20:50:00	2.85 PMT
041014A	NAOC2.16	14	11:23:30	8.49 PMT
korea-003	BOAO1.8	14	10:55:16	7.27
lit-05	Moletai1.56	14	19:00:10	7.37 PMT
korea-004	BOAO1.8	15	10:19:00	7.75
A0934	McDonald2.1	15	06:26:07	2.65
NOT-001	NOT 2.6	15	19:55:23	4.32
NOT-002	NOT 2.6	16	00:19:52	4.87
lulin-0008	Lulin1.0	16	12:34:26	6.45
NOT-003	NOT 2.6	16	19:43:22	8.37
rkb1*	LNA1.6	17	02:25:04	3.15
A0939	McDonald2.1	17	05:19:58	1.04
A0940*	McDonald2.1	17	07:32:18	1.32
lulin-0010	Lulin1.0	17	11:36:36	7.51
maja10182004	KPNO2.1	18	09:06:40	1.78
lulin-0012	Lulin1.0	18	10:50:02	3.10
041018B	NAOC2.16	18	13:47:00	5.88 PMT
maja10192004	KPNO2.1	19	05:19:40	3.40
lulin-0015	Lulin1.0	19	10:43:11	8.33
maja10202004	KPNO2.1	20	02:11:20	3.18
maja10202004b	KPNO2.1	20	09:39:40	0.93
lulin-0016	Lulin1.0	20	11:35:48	7.35
hungary-007*	Kolkony Obs.1.0	20	18:09:56	1.56

CHAPTER 4. The frequencies of PG0014+067

4.1 Summary of previous observations of PG0014+067

PG0014+067 was found to be a pulsating sdB star by the Montréal group, who followed up with several nights at the CFHT in 1998. The results of their 1998 runs have been published (Brassard et al. 2001). These authors isolated 16 harmonic oscillations (with the resolution of 2.8 μHz) in the white light photometric data on PG0014+067 gathered with the LAPOUNE PMT photometer attached to the 3.6 meter Canada-French-Hawaii Telescope (CFHT) obtained during 5 consecutive nights in 1998, with an average run length of three hours or less. The periods of the modes range from 80.73 to 169.90 seconds, while the amplitudes are all below 3 mma.

The pulsations in this low amplitude, multimode pulsator are associated with the normal acoustic p-modes. Among those 16 frequencies, they found three closely spaced frequency doublets with the average splitting of $\Delta f \sim 9.5\mu$Hz, from which they estimated the rotation period of PG0014+067 to be $P_{rot} \simeq (\Delta f)^{-1} = 29.2 \pm 0.9$ hr. Furthermore, as they see combination frequencies in the high frequency domain, they speculate on possible nonlinear structure.

This high number of modes in such a relatively narrow frequency range posses a fundamental challenge to the theory of nonradial pulsations in these stars, as there are not enough radial and nonradial modes with low degree ℓ ($\ell < 3$) to account for all 16 without rotational splitting. One proposed solution to such a large numbers of modes involves high degree (ℓ) modes. These authors show a model for which $M =$

$0.49 \pm 0.02 M_{\odot}$ assuming a high degree modes ($\ell = 0, 1, 2, 3$) for the oscillation modes derived from the models themselves.

Because of the time sampling of the data, these single site data suffer from severe 1 cycle per day aliases (explained in Chapter 2). The frequency set obtained by Bressard et al. (2001) is limited because of aliasing in the temporal spectrum due to the daily gaps in the data. Because of this the aliases may be mistakenly identified as the true frequencies rather than the real ones. This becomes a real issue when trying to identify modes of lower amplitudes.

4.2 Frequency analysis of the WET data set on PG 0014+067

Combining all the light curves described in the previous chapter (Figure 3.2) the Fourier transform (FT) was computed to deduce the periodicities present in the data. The FT of the full data set on PG0014 gathered during Xcov24 is depicted in Figure 4.1 showing the 'modulation amplitude', in units of mma= ma/1000, where ma=$\Delta I/I$, of variations in the detected intensity I at a given frequency. The spectral window shows the pattern that would be produced by a single, noise-free periodicity, taking the sampling intervals and gaps from the real data. Figure 4.2 shows the spectral window of the whole WET run on PG0014.The central peak in the plot corresponds to the input frequency of the sinusoid (7000μHz in this case) and all other peaks on either side are aliases caused by the gaps in the data set. For a detailed discussion on aliases see Section 2.3.2.

Our Fourier transform can reveal frequences up to the Nyquist frequency, $f_N = (2\Delta t_{cycle})^{-1}$, where Δt_{cycle} is the cycle time, i.e. the time between two consecutive data points. In our case the data with different cycle times, from 5 to 25 seconds, were combined. Therefore I used the averaged cycle time of 15 seconds, which gives the Nyquest frequency of $f_N \approx 30000\mu$Hz.

As can be clearly seen in Figure 4.1, the main action is concentrated in a very narrow frequency range. It appears as if all the power is distributed into two to three modes around the 7000 μHz with the maximum intensity variations of $\sim$ 3 *mma*. This is a typical signature of a low amplitude sdB pulsator. Figure 4.1 confirms that there are no frequencies with amplitudes above the mean noise level at higher frequencies, up to the Nyquist frequency. Therefore, we can securely focus our analysis on the narrow band of the main power.

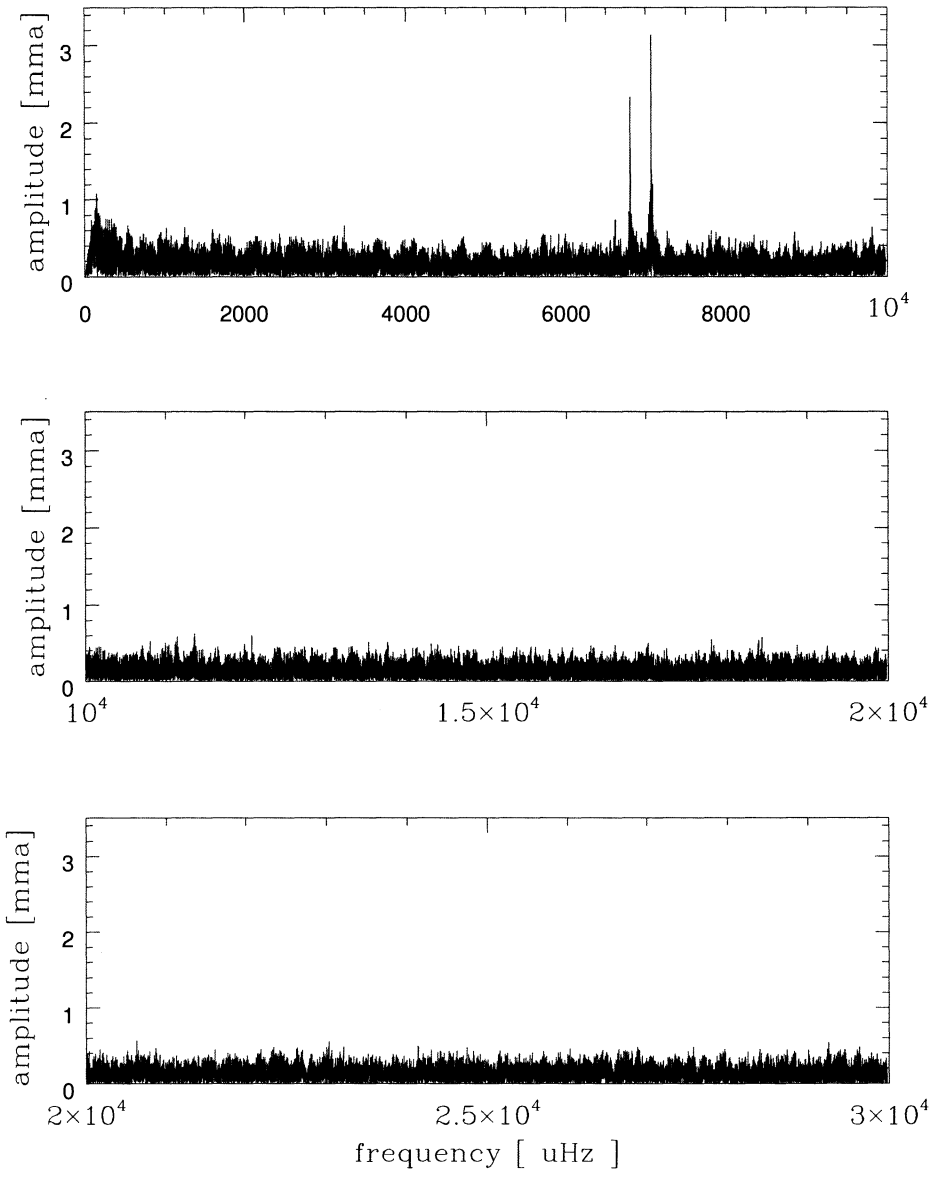

Figure 4.1 Weighted Fourier transform of the complete WET data set on PG0014+067.

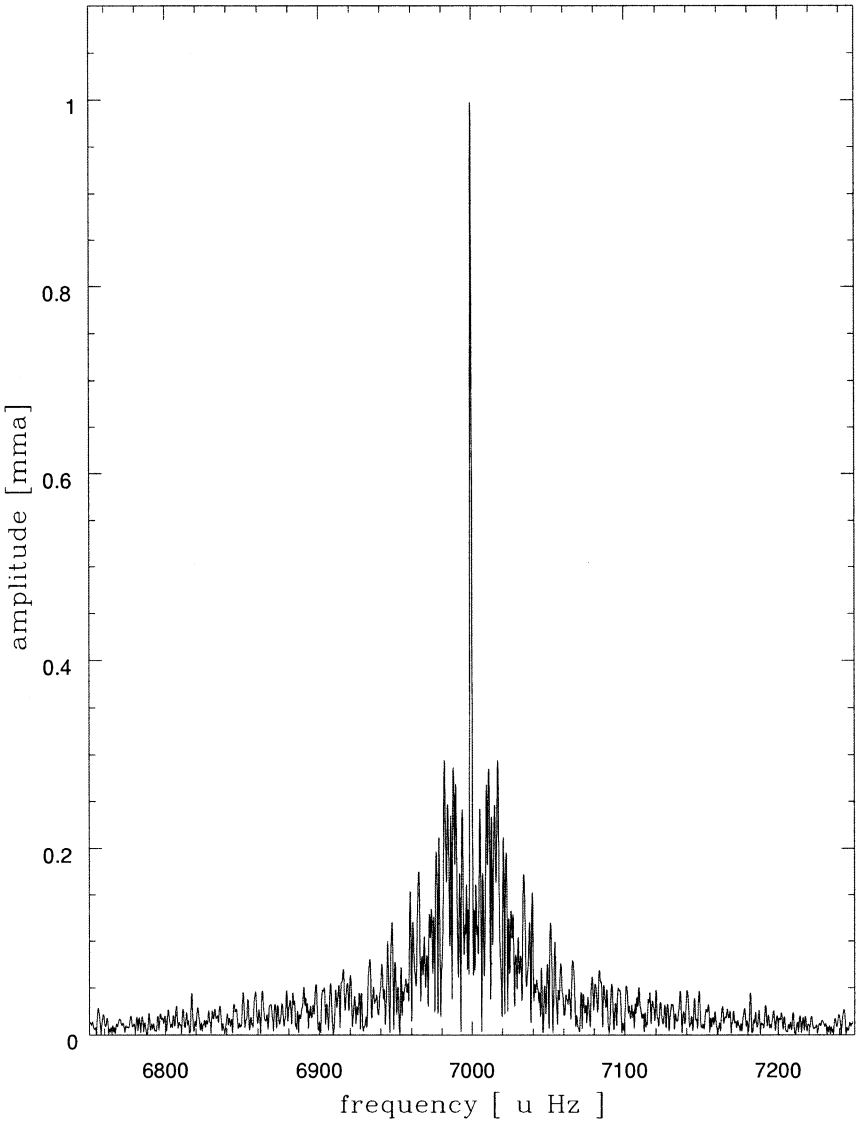

Figure 4.2 Spectral window for the PG0014+067 WET data set.

Figure 4.3 expands the FT of the entire data set around the region of the main power, 5 000-10 000μHz. As an objective criterion for determining which peaks are real signals in the power spectrum, I adopt a conservative significance threshold at $3.7\sigma_{noise}$. Since power is the square of the amplitude, the average power out to the Nyquist frequency is a measure of the mean-square deviation from zero amplitude. The square-root of

this value is the root-mean-square amplitude of the noise, i.e. the standard deviation σ_{noise}. The solid white line in Figure 4.3 corresponds to the noise level σ_{noise}, and the corresponding red (dark) line represents $3\sigma_{noise}$. While peaks with the amplitude below the adopted threshold of $3.7\sigma_{noise}$ were not accepted in this analysis, the well behaved isolated peaks seen above the $3\sigma_{noise}$ limit, which correspond to 99.7 % confidence level (Metcalfe et al. 2005), are tabulated in Table 4.2. This is the threshold many scientists find in practice as sufficient to account for the reality of a mode (Brassard et al. 2001, Metcalfe et al. 2005, Charpinet et al. 2005). Hence, for comparison we show this lower threshold line (given in red) in the graphs.

The noise in the power spectrum is calculated by averaging the amplitudes around each frequency in a wide frequency range. This frequency range was 4/5 of the entire frequency range. This was done to sample the noise through the different frequency domains more realistically. More precisely, if we were to calculate the simple average amplitude over the entire data set, the noise from the sky transparency variations dominating the low frequency regime would have "artificially" increased the noise at the higher frequencies, and vice versa.

4.3 Weighting

PG 0014 was observed with telescopes between 0.9 and 2.56 meters in aperture. The contribution of the small telescopes to the combined WET results can be very important. As shown by Handler (2003), if they improve the spectral window, they can reduce the effective noise in the total FT by more than their light gathering power would imply. To optimize the number of detected intrinsic frequencies present in the total light curve, gathered with the different aperture telescopes, we have to optimize the signal-to-noise ratio of the signals in the FT and the window function. Therefore, the weighting scheme favored by Handler (2003) was used: weights are determined for individual runs- with

the weight for a run taken as inversely proportional to the mean point-to-point scatter within the run.

A comparison of weighted and unweighted data is shown in Figure 4.4. The weighted temporal spectrum shows a considerable improvement over the unweighted one. As an obvious example, consider the peaks at 5924 μHz and 6193 μHz. Those are seen clearly in the weighted FT. Also, signals around 6630 μHz and 7300 μHz are much better exposed in the upper panel (weighted data). However, to some degree, weighting inflates the amplitude of the daily aliases and widenes the peaks. Consequently, weighting may affect the ability to resolve closely spaced peaks. Bearing this in mind weighted data were used to expose and identify periodicities, but the frequencies, amplitudes and phases of the individual peaks were determined using the 'unweighted' data.

4.4 Down to the beat - isolating the pulsations from the light curve of PG 0014

Although the amplitude spectrum (Figure 4.1) does not appear very complex, attempts to determine the underlying variations by prewhitening reveal that this star indeed has a complicated pulsation spectrum. Some of the frequencies found in this star are close together, yet not equally spaced, making us not forget the words of one of the founders of WET Nather et al. (1990): "interpretation of the combined alias patterns introduced by the presence of several frequencies is at best difficult, and often impossible". This was seen in the very first steps of the frequency analysis, while trying to identify the highest amplitude peak in the data. An unresolved pair of frequencies (or group of closely spaced frequencies) will cause the apparent amplitude and frequency of the unresolved peak in the power spectrum to change with time as the underlying components beat with one another, and the beat period (the time required to go from constructive interference to destructive interference and back again) can be as long as

several days. Therefore, the run must be longer than the longest beat period in order to resolve the individual frequencies present. The WET run on PG0014 spans two weeks which results in a formal frequency resolution of $\Delta\nu = 0.9\mu$Hz.

After identifying the highest amplitude peak in the (computed) weighted power spectrum of the original data set, we go back to the unweighted FT to confirm the periodicity. We then remove this peak from the data by subtracting a sine wave (with the frequency, amplitude and phase determined by non-linear least-squares fit) from the light curve. We calculate the power spectrum of the residuals (light curve of the entire data set with this sinusoid removed). Then we look at this "prewhitened" weighted FT to find the next highest peak and repeat the procedure. We determine the values of frequencies step by step, carefully checking whether new frequencies affect the other values and adjusting them, if necessary, by calculating a simultaneous n- frequency fit to the data until no new peaks could be identified with significance (with amplitude above $3.7\sigma_{noise}$).

Figure 4.5 illustrates this procedure. The FT of the entire data set in the region around the highest amplitude peaks is shown in the middle panel, while the spectral window centered at 7000μHz in given at the top panel. The prewhitened FT by the two highest peaks, $f_1 = 7088.67\mu$Hz with amplitude of 3.0 mma and $f_2 = 6926.06\mu$Hz with amplitude of 2.4 mma is presented at the bottom of Figure 4.5.

Simple comparison of the spectral window (top panel) with the FT (middle panel) shows that the highest peak f_1 is more complex than the simple window pattern formed by a single periodicity, indicating either possible closely spaced frequencies or some random amplitude modulation of the pulsation. On the other hand, the power around the 6826μHz resembles a pattern of the window, suggesting that this might be one of the "clean" modes.

Looking at the residual power spectrum (at the bottom of Figure 4.5) we see that this is indeed the case. All of the power around the f_2 mode is gone after prewhitening, confirming that this is a single mode, but there is still lot of power remaining above

$3\sigma_{noise}$ level (red/dark solid line) after removing the highest peak at 7088.67μHz.

The highest amplitude peak f_1 appears to have fine structure with two additional closely spaced peaks at frequencies $f_3 = 7091.0\mu$Hz and $f_4 = 7091.7\mu$Hz and amplitudes of 1.2 *mma* and 1.1 *mma* respectively. Even though this frequency difference is formally unresolvable given our frequency resolution of 0.9μHz, both of these modes are easily resolved in NLLS fit to the data. Furthermore, all the power above $3\sigma_{noise}$ level (red solid line) is gone after prewhitening the data with those three peaks. Figure 4.6. illustrates this procedure, by showing the FT of the data before (top) and after removing f_3 and f_4 (bottom).

The next highest peak in the FT is at 7289.0μHz. Figure 4.7 displays this region of the frequency domain, showing the FT of the data before (top) and after (bottom) removing this periodicity, with the parameters determined by the NLLS fit to the data. Although there are some power left above the 3σ level (red/dark solid line) NLLS cannot satisfactorily converge on the parameters of these low amplitude peaks. Hence, prewhitening stops here for this region, but we do indicate this peak as a possible real frequency, see discussion in Section 4.3 and Table 4.2.

The next highest amplitude region is around 6632μHz. Figure 4.8 shows this region, where the top panel gives the residual FT after five highest peaks have been removed (f_1 to f_5). The highest peak on the upper plot consists of two closely spaced modes at $f_6 = 6632.8\mu$Hz with the amplitude of 0.6*mma* and $f_8 = 6631.9\mu$Hz with the amplitude of 0.5*mma*. The frequency difference between those two modes is at the order of our resolution, 0.9μHz. After those two sinusoids have been removed from the lightcurve, the residual spectrum stays "clean", as is shown on the middle panel of Figure 4.8. The next highest peak here is at $f_9 = 6452.9\mu$Hz with an amplitude of 0.4*mma*. Removal of this peak shows no power left above the noise (the bottom panel on Figure 4.8). The only power left in this region is at 6670μHz, but at an amplitude that is below the adopted threshold, albeit above the $3\sigma_{noise}$ level. We cannot confirm this frequency is

real, we do however indicate this frequency in our "almost" list (Table 4.2).

At the low frequency end, there is a peak with a rather low amplitude, at about 5923μHz. Just by comparing with the spectral window (Figure 4.2) we see that we are most probably dealing with the two closely spaced frequencies. The NLLS however finds a mode with the amplitude of $0.5mma$ at $f_7 = 5923.4\mu$Hz. Figure 4.9 shows this region, giving the temporal spectrum before (top) and after this mode is removed by prewhitening (bottom panel). There is still excess power left after its removal, with the frequency of a possible mode at 5921.3μHz. NLLS is unable to converge on a simultaneous fit to these two modes along with the nine found previously. This frequency is included in to the list of possible true periodicities (Table 4.2, Section 4.3).

Now we look again at the bigger picture to see if there are still some significant peaks left after we have prewhitened by these nine (f_1 to f_9) modes simultaneously. Figure 4.10 spans the main power domain showing the original FT of the entire WET data set at the top, followed by the FT of the data prewhitened by the above nine frequencies. The blue(top) solid line is our adopted threshold ($3.7\sigma_{noise}$), the red (next down) solid line is the $3\sigma_{noise}$ level, while the white solid line is the average noise as explained at the beginning of this section.

The only peak that sticks above the blue line is just below 6200μHz. The attempt to find the NLLS fit to the data including this mode was succesful despite its low amplitude, and we have therefore removed this peak with the frequency of f_{10}=6193.5μHz and amplitude of $0.4mma$ from the total lightcurve. Prewhitening successfully removes all the excess power with only the noise left in that region. Figure 4.11 shows the FT of the residuals. Again, at the top of the figure we have the starting spectrum, in this case the residual FT prewhitened by the nine frequencies found, and the bottom is the FT after we have removed the ten frequencies.

4.5 Conclusions

By performing the Fourier analysis and NLLS fitting on the entire WET data set obtained during the Xcov24, we have detected a total of ten frequencies in the power spectrum of PG0014+067 with the 99% significance level and with the resolution of 0.9μHz.

Table 4.1 Periodicities found in WET data on PG0014+067.

Mode	**Frequency** [μHz]	**Period** [s]	**Amplitude** [mma]	T_{max} [s]
f7	5923.4 ±0.1	168.821 ±0.003	0.54 ±0.13	20 ±16
f10	6193.5 ±0.2	161.458 ±0.005	0.44 ±0.13	125 ±20
f9	6452.9 ±0.2	154.968 ±0.005	0.45 ±0.13	150 ±18
f8	6631.9 ±0.2	150.786 ±0.005	0.49 ±0.15	90 ±20
f6	6632.8 ±0.1	150.766 ±0.003	0.65 ±0.15	143 ±15
f2	6826.06 ±0.03	146.4974 ±0.0006	2.38 ±0.13	28 ±3
f1	7088.67 ±0.03	141.0702 ±0.0006	2.98 ±0.13	149±3 *
f3	7091.0 ±0.1	141.023 ±0.002	1.22 ±0.33	133±11
f4	7091.7 ±0.1	141.011 ±0.002	1.10 ±0.32	55±11
f5	7289.0 ±0.1	137.193 ±0.002	0.65 ±0.13	107±11

The final results of a simultaneous multiple sine-wave fit to the total light curve are summarized in Table 4.1, listing the frequencies, amplitudes and phases of the main modes detected in the WET data set. The column labeled as **Mode** relates to the relative amplitudes of the found periodicities. The column labeled as T_{max} is the phase, i.e. the time of the first maximum after August 21 2004 0 UT, given in seconds. For the T_{max} marked with asterisks, the period is added to match among all individual runs. The actual value for the phase of f1 for the entire light curve is 8 ±3. The uncertainties for the values given in the table are formal least-square estimates of the 1σ errors.

There are eleven low amplitude peaks that nearly reach the adopted threshold ($3.7\sigma_{noise}$). Had we adopted somewhat less conservative acceptance criterion at $3\sigma_{noise}$, for the reality of the mode, these modes would have been accepted as real if we could converge a NLLS fit. Therefore, these peaks are indicated as marginal detections. Table

4.2 lists the frequencies, corresponding periods and amplitudes of those eleven marginaly detected modes. Figure 4.12 shows the FT of the combined WET data set on PG0014 before (top) and after the removal (bottom) of ten modes listed in Table 4.1. The marginally detected signals listed in Table 4.2 are apparent in the residuals as the peaks in between the blue (top) and red (next down) solid line on the bottom of Figure 4.12.

Table 4.2 Marginal detections- peaks with the amplitude between $3.7\sigma_{noise}$ and $3\sigma_{noise}$ seen in WET data on PG0014.

Frequency [μHz]	**Period** [s]	**Amplitude** [mma]
5921.3	168.882	0.40
5973.5	167.406	0.38
6674.0	149.835	0.43
7278.9	137.383	0.40
7895.0	126.662	0.39
7938.3	125.971	0.45
8870.8	112.729	0.42
9576.6	104.421	0.41
9834.2	101.686	0.38
12083.7	82.756	0.37
13539.8	73.856	0.38

In partial support of the run, six nights of observation of PG0014 took place two months prior to Xcov24 (August 2004) using the high-speed multi-channel photometer ULTRACAM (Dhillon et al. 2005) on the 4.2m William Herschel Telescope (WHT) at La Palma by Simon Jeffery and Conny Aerts (Jeffery et al. 2005 in press). The first frequency in the Table 4.2 at 5921.3μHz is seen in the ULTRACAM data (Aerts C., private communication) and therefore has a higher probability of being a real signal.

Before proceeding into the next chapter we compare our results with those from Brassard et al.(2001), the only published ones on PG0014 so far. Table 4.3 lists the periodicities identified by Brassard et al. (2001). The formal errors in frequency or period are not given in the paper, but the probable accuracy is estimated to be 0.28μHz.

Comments on the comparison are detailed in the last column (**Note**), showing in bold the modes found in the WET data set from Table 4.1.

Table 4.3 Periodicities identified by Brassard et al. (2001) data on PG0014+067-taken from Table 2 of their paper. The column **Note** compares it with the WET data, with the frequencies listed in bold corresponding to our Table 4.1.

Mode	**Frequency** [μHz]	**Period** [s]	**Amplitude** [mma]	**Note**
$\nu 1^-$	5896.2	169.60	0.388 $\pm$0.088	not seen in WET data
$\nu 1^+$	5923.2	168.83	0.481$\pm$0.088	seen in WET data **f7**
$\nu 2$	6227.7	160.57	0.390$\pm$0.086	3 c/day away from **f10**
$\nu 3^-$	6621.1	151.03	2.183$\pm$0.087	1 c/day away from **f6**
$\nu 3^+$	6630.7	150.81	0.548$\pm$0.088	seen in WET data **f8**
$\nu 4$	6837.5	146.25	1.7229$\pm$0.087	1 c/day from **f2**
$\nu 5^-$	7079.1	141.26	0.393$\pm$0.093	1 c/day from **f3**
$\nu 5^+$	7088.7	141.07	1.950$\pm$0.090	seen in WET data **f1**
$\nu 6$	7150.2	139.86	1.435$\pm$0.094	not seen in WET data
$\nu 7$	7286.2	137.25	0.318$\pm$0.087	seen in WET data **f5**
$\nu 8$	7670.3	130.37	0.281$\pm$0.087	not seen in WET data
$\nu 9$	7952.1	125.75	0.466 $\pm$0.086	not seen in WET data
$\nu 10$	8552.1	116.93	0.312 $\pm$0.086	not seen in WET data
$\nu 11$	9797.6	102.07	0.337$\pm$0.086	not seen in WET data
$\nu 12$	9970.3	100.30	1.061$\pm$0.086	not seen in WET data
$\nu 13$	12386.8	80.73	0.462$\pm$0.086	not seen in WET data

Note that 8 out of 10 modes found in the WET data set (Table 4.1) are also present in Brassard et al. (2001) within the cycle per day aliases. The only two of our modes not apparent in their data are $f4$ and $f9$. The $f4$ frequency is part of a closely spaced multiplet which is unresolvable with the resolution they had (2.8μHz). The mode at $f9$ might have had a lower amplitude at the time of their observations, since the power spectrum of pulsating sdB stars is known to change over time, from year to year and even from season to season in some cases (Kilkenny et al. 1999).

Now, after true periodicities of PG0014 are securely identified, can we proceed further into testing the theoretical expectations discussed in Chapters 1 and 2. The main questions raised are: does this rich power spectrum fit nicely into the high ℓ model put

forward by Brassard et al. (2001), or can we explain it within the proposed theory of fast rotation of the inner core via large rotational splitting in the observed modes?

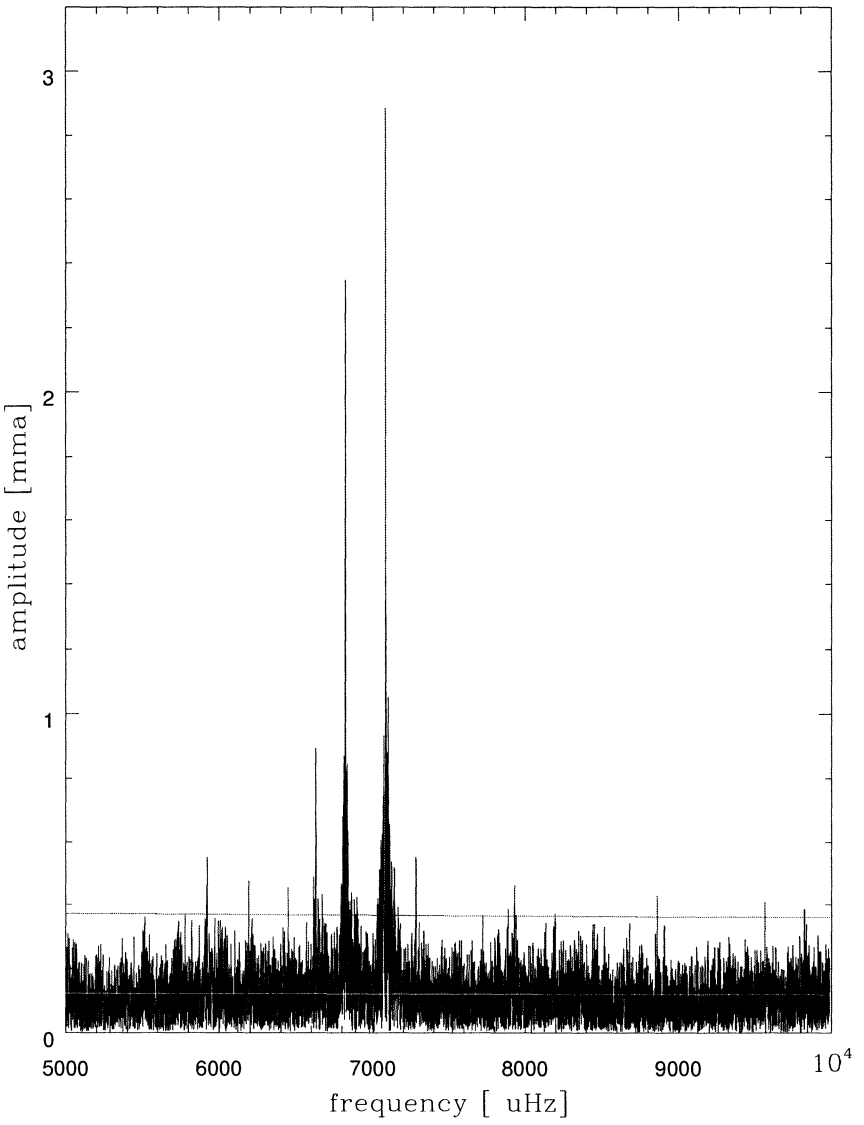

Figure 4.3 Weighted FT of the PG0014 WET data expanded to the region of the most power.

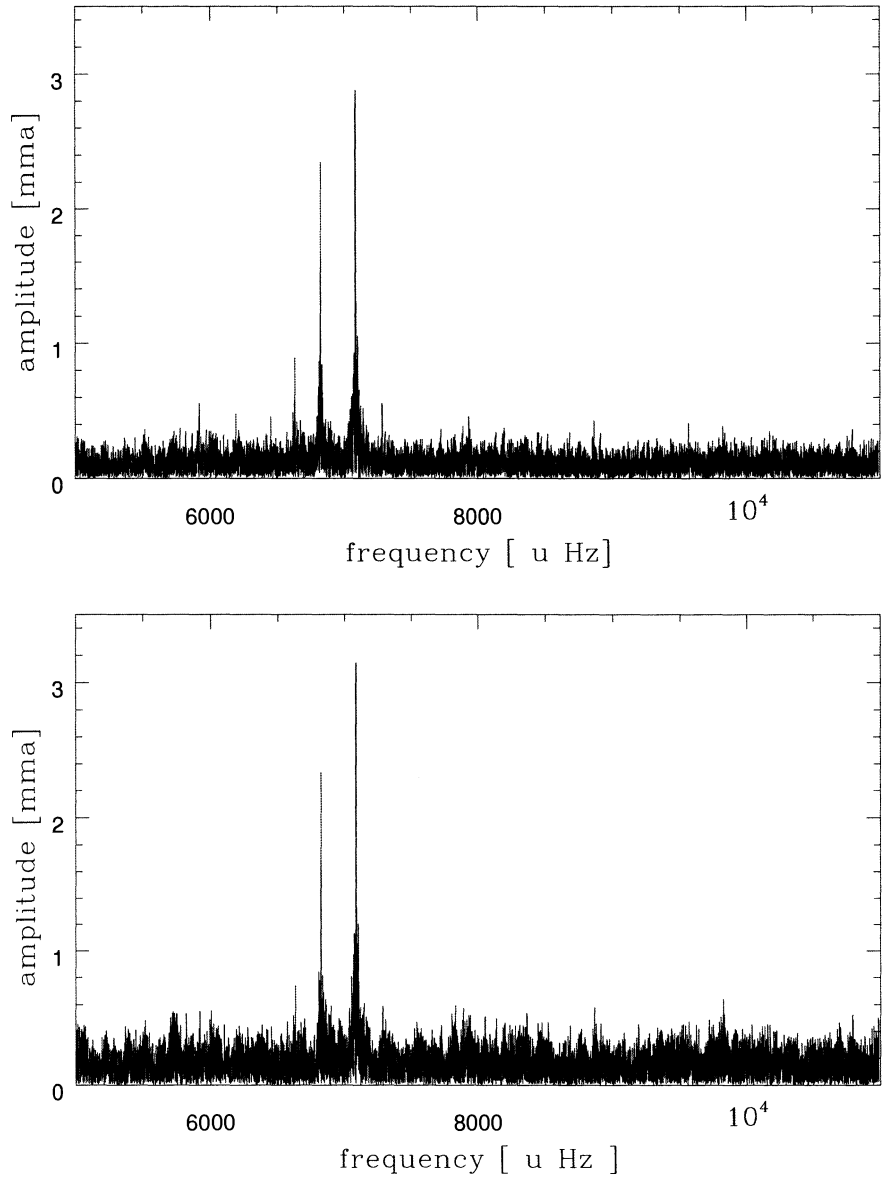

Figure 4.4 Upper panel: weighted FT of the full data set on PG0014 in the range of the most power. Lower panel: "unweighted" FT of the same data set at the same scale.

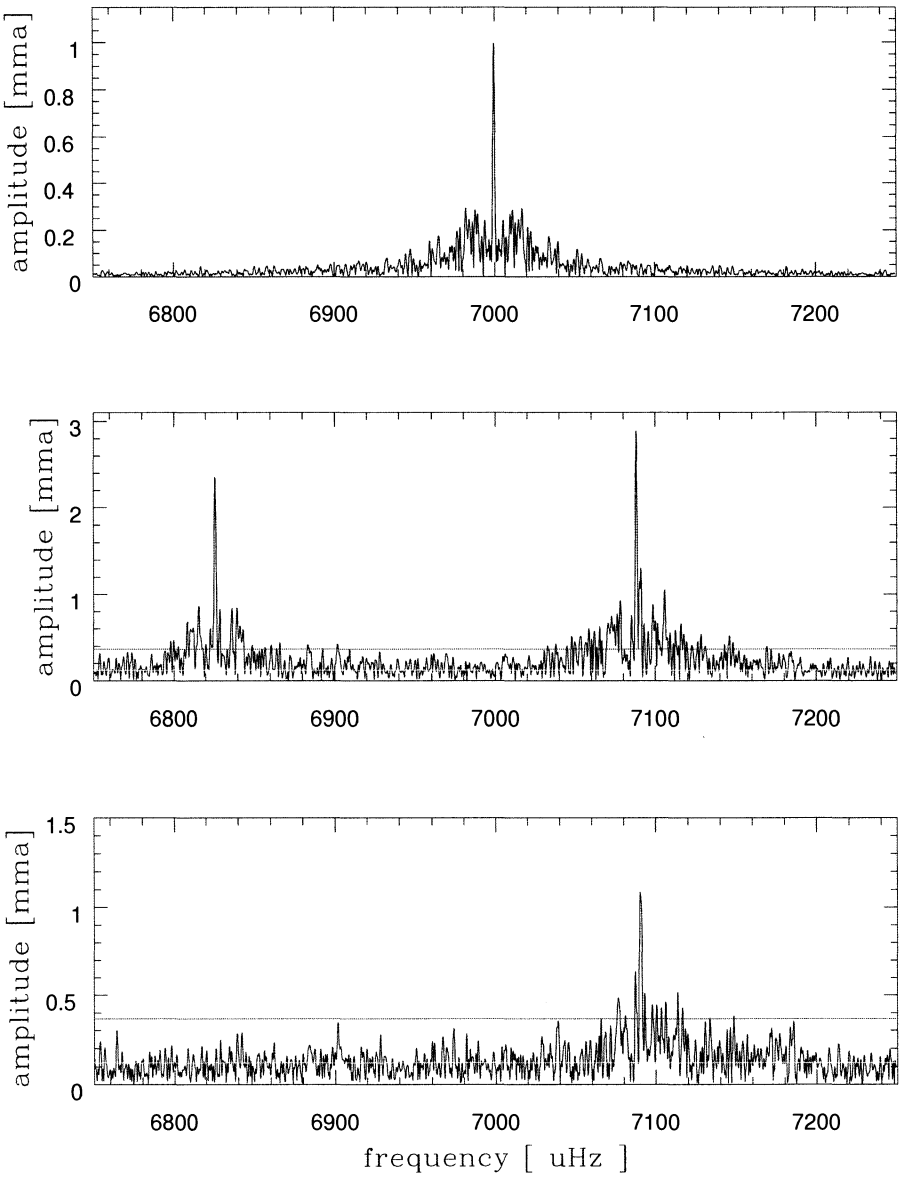

Figure 4.5 Top panel: the spectral window centered at 7000μHz given on the same frequency scale as the data. Middle panel: the FT of the entire WET data set on PG0014 expanded around the highest power. Bottom panel: the residual FT prewhitened by f_1 and f_2 all on the same frequency scale. Note the different amplitude scale.

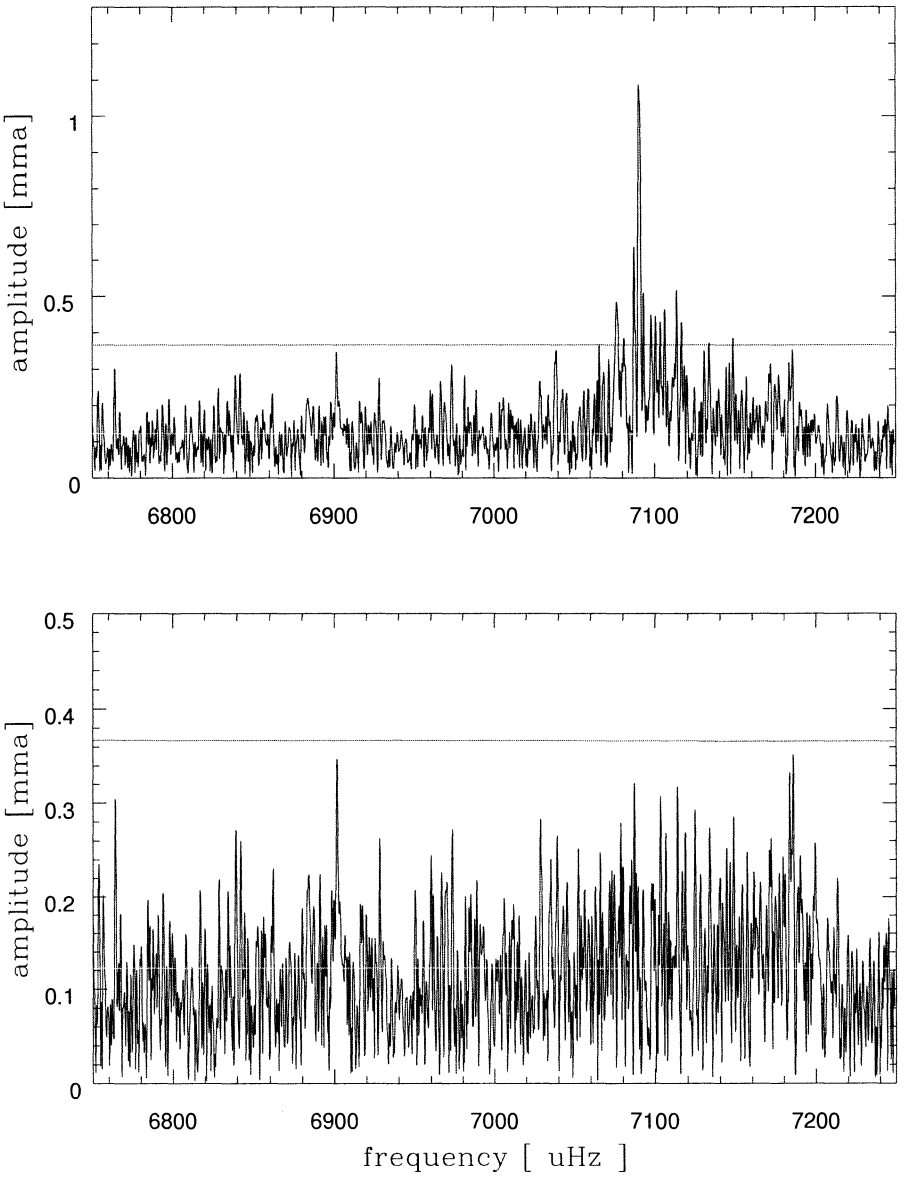

Figure 4.6 Top panel: the prewhitened FT by f_1 and f_2. Bottom panel: the residual FT after removing the additional two modes, f_3 and f_4. Note the different amplitude scale.

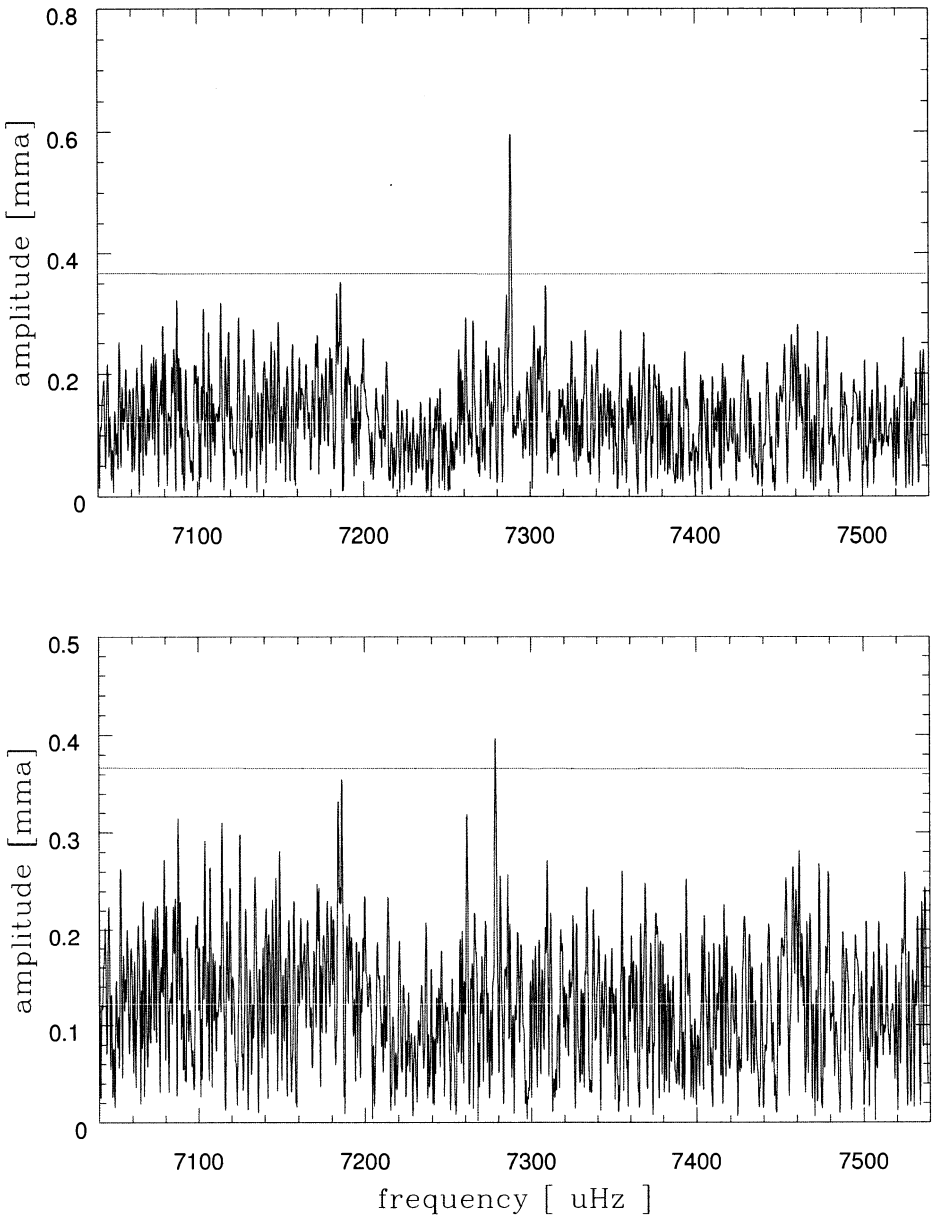

Figure 4.7 Top panel: the FT of the entire data set expanded around f_5. Bottom panel: the residual FT after prewhitening with $f_5 = 7289.0\mu$Hz.

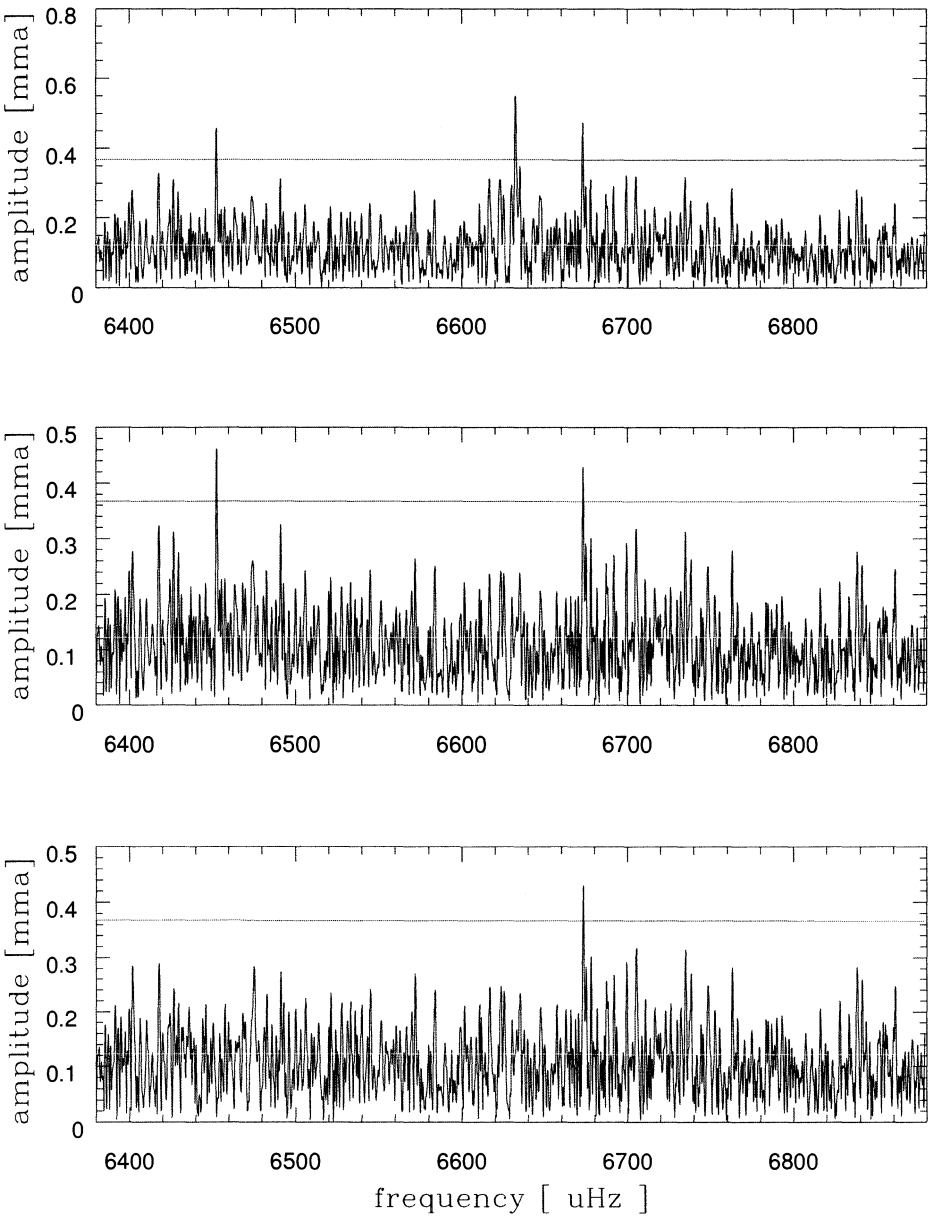

Figure 4.8 Top panel: the residual FT after the first five modes have been removed from the data. Middle panel: the temporal spectrum after $f_6 = 6632.8\mu$Hz and $f_8 = 6631.9\mu$Hz have been removed. Note the change in amplitude scale. Bottom panel: the FT prewhitened by the $f_9 = 6542.9\mu$Hz.

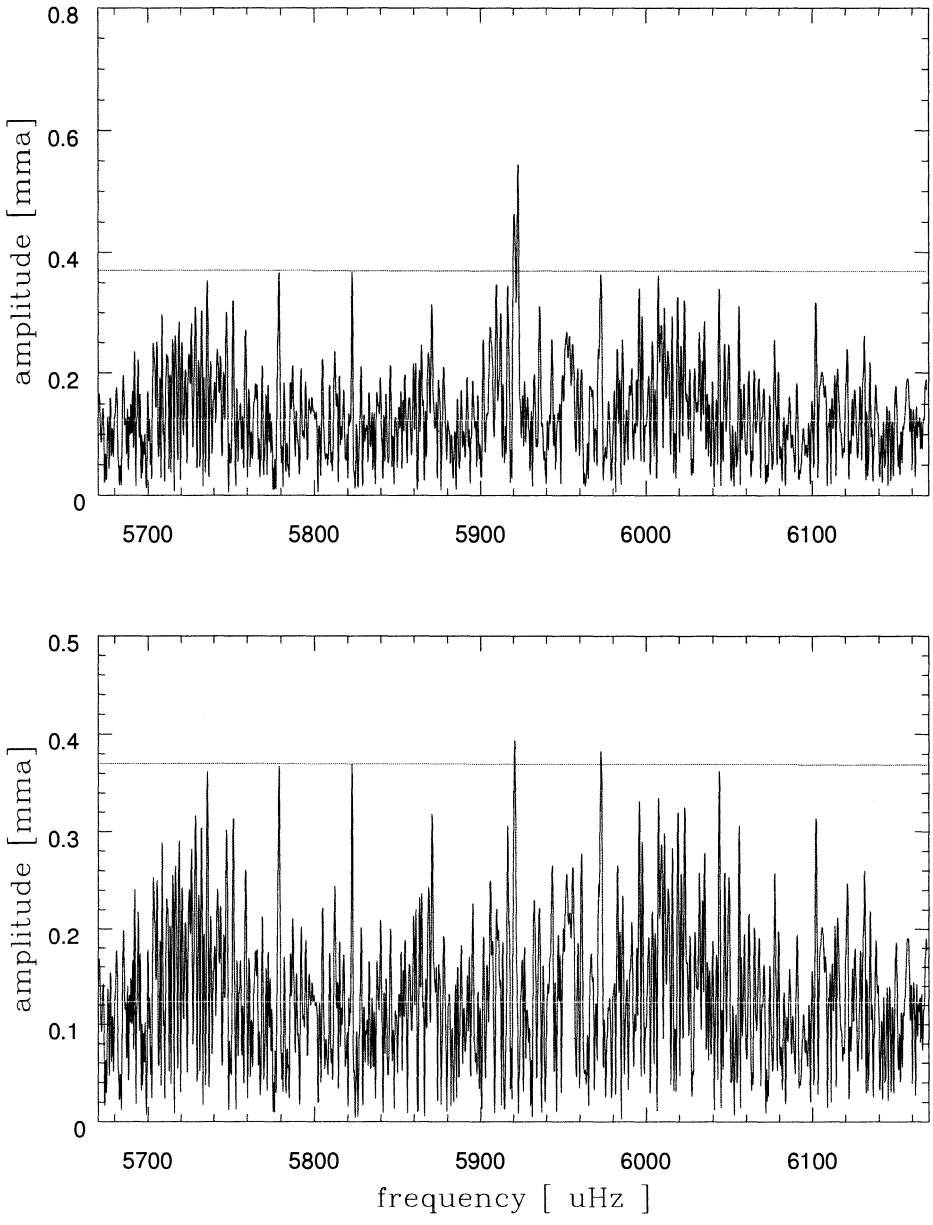

Figure 4.9 The FT of the entire data set at the low frequency end of the main power (top), followed by the residual FT prewhitened with the f_8 (bottom).

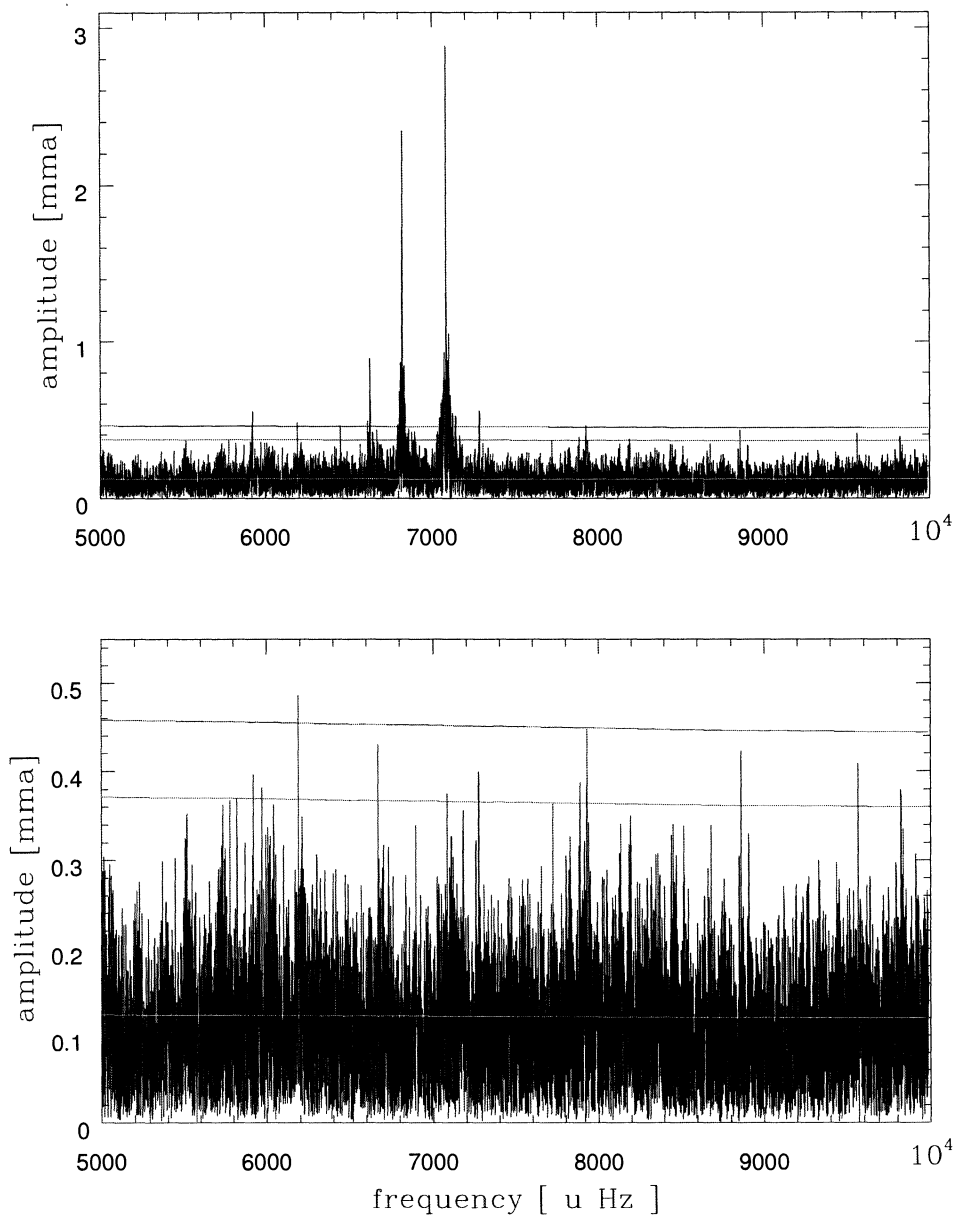

Figure 4.10 The original FT (top) followed by the residual FT (bottom) after the removal of the nine modes (f_1 to f_9). Note that the red (lower) solid line corresponds to $3\sigma_{noise}$, while the blue (upper) solid line corresponds to $3.7\sigma_{noise}$. The amplitude scales are different.

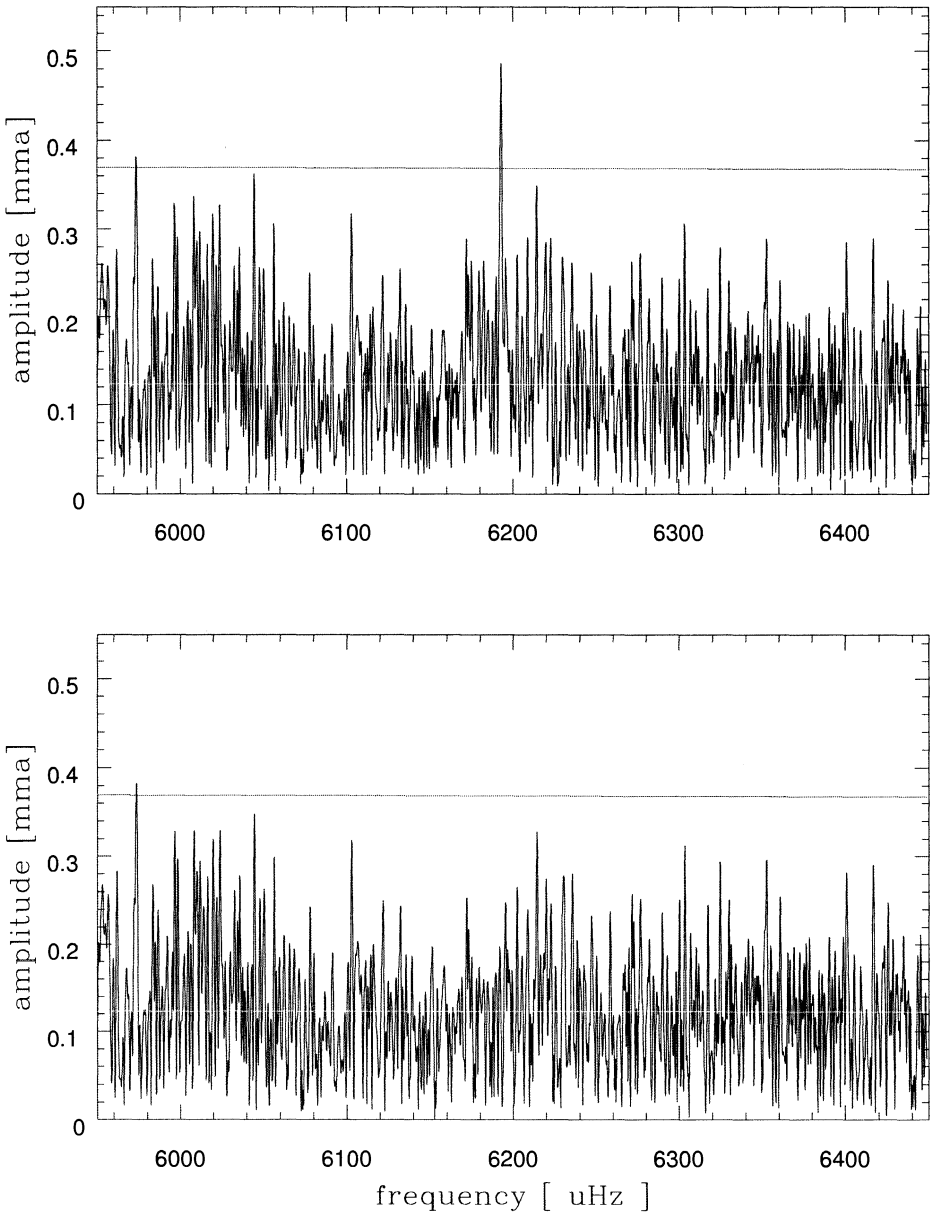

Figure 4.11 FT near f_{10} prewhitened by the nine frequencies, f_1 to f_9 (top) followed by residual FT after removing the tenth frequency f_{10} (bottom).

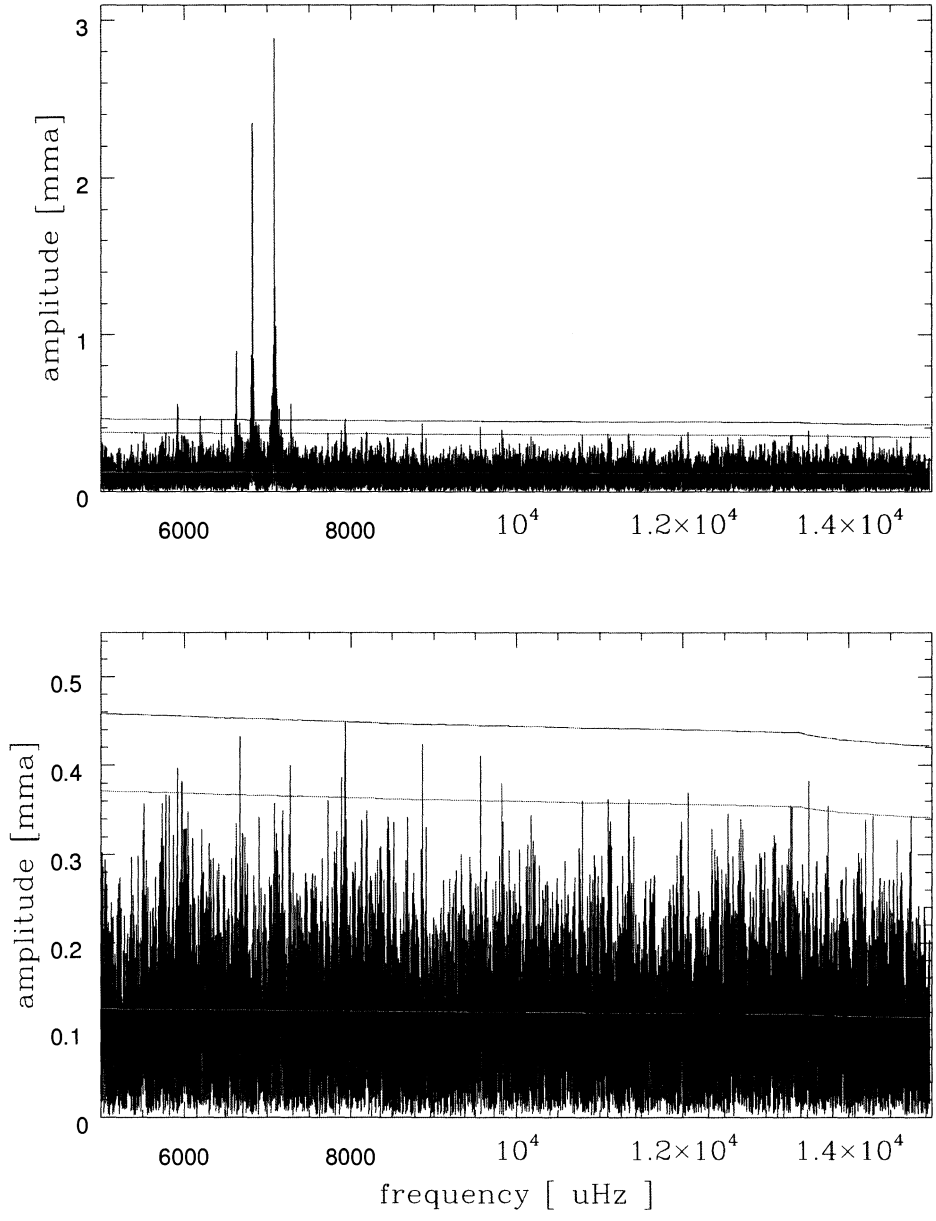

Figure 4.12 Total FT of the original WET data set on PG0014(top) followed by the residual FT of the same data set, prewhitened by the ten frequencies listed in Table 4.1. Note that the red (lower) solid line corresponds to $3\sigma_{noise}$, while the blue(upper) solid line corresponds to $3.7\sigma_{noise}$. The white solid line is σ_{noise}.

CHAPTER 5. Summary and discussion

Chapter 4 revealed secure frequencies of pulsation of PG0014 letting us delve further into the issues introduced in the beginning of this work. First, we do a check to see how stable these modes are; then we will use the frequencies found (Table 4.1) to see what answer we can find to the questions raised in Chapters 1 and 2, i.e. high ℓ modes or broad rotational splittings? Also, the other issue one has to address in analyzing the stellar pulsations is are these modes "well behaved" of do they show phase effects that could result from orbital modulation, beating effects, etc. ?

5.1 Stability of the modes

We note that complexity in the FT could result from timing errors in the data or/and stochastic behavior in the modes. Modes of relatively high amplitude allow us to check the phase and amplitude stability. There were only two modes high enough in amplitude ($>$ 1 mma) to be resolvable in each individual run of the WET data set. Therefore, we have been able to check the stability of only those two periodicities, namely f1 and f2.

To determine the phases (which we denote by $T_{\max}$, the time of the first maximum for that periodicity in the run) and amplitudes for the observed pulsations as a function of time, we first reduce the data as described in Chapter 2. Then we use the combined lightcurve of the entire data set to find the best period as described in Chapter 4. Then, using the best period as a fixed parameter, the phases and amplitudes for subsets of the entire data set are determined using LSQ.

Having the amplitudes and phases of each frequency determined for each individual run, we can compare them on a night to night basis. Figures 5.1 and 5.2 show the amplitudes and phases for f_1 and f_2 of each run in the WET data set. The time on the abscissa is in seconds starting from August 21 2004 0 UT. The errors on amplitudes and phases for some runs are very high. This is because of either a small signal-to-noise ratio (smaller telescope or non-photometric night) or the small number of points (short run) in the particular run. We cannot do much about the size of the telescope and the bad sky conditions, but we can make some improvement on the latter one. Combining the runs that are taken closely in time we can decrease the error on the computed amplitude and phase at the expense of time resolution in the plot. This is shown on Figures 5.3 and 5.4 where the the subsets of data (close enough in time) have been examined, rather that each individual night.

The first thing to notice in those figures is that both the amplitude and the phase of f_1 appear to vary on the same time scale of about 5 days. During the WET campaign as the data were coming in, we have noticed that the dominant mode had different amplitude from one run to the next, as it was not always the highest peak in the FT. Therefore it is not surprising that we see this almost a sinusoidal variation of the amplitude and phase of f_1 mode. The situation is more stable for the second mode f_2, as it appears to be constant both in amplitude and phase through out the run. Unfortunately, we have only few data points with very high errors at the beginning of the run caused by the very bad weather conditions, which increases the scatter.

If what we see in f_1 is a variability of phase and amplitude with time, there are two possibilities. The variability can be the true instrinsic mode variability or more probably the beating of closely spaced modes. The analysis in Chapter 4 (standard FT / NLLS) assumes that the frequencies and amplitudes are constant stationary.

Even though the scatter in the above figures (phase and amplitude) seems to be not entirely random, the errors are too high to make any claims, especially in the first part

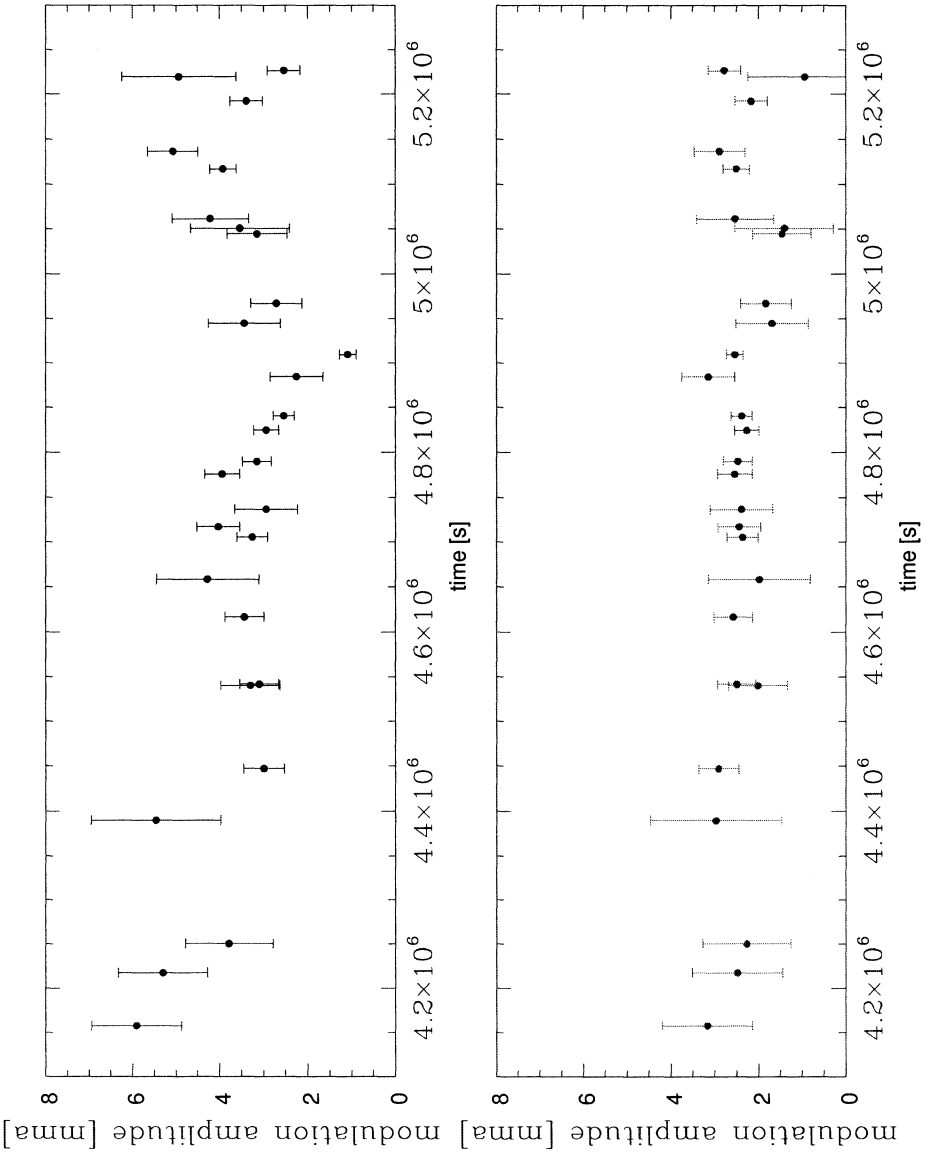

Figure 5.1 The ampitudes of the two best resolved modes f_1 on the top and f_2 is the bottom one (in red) for each individual run.

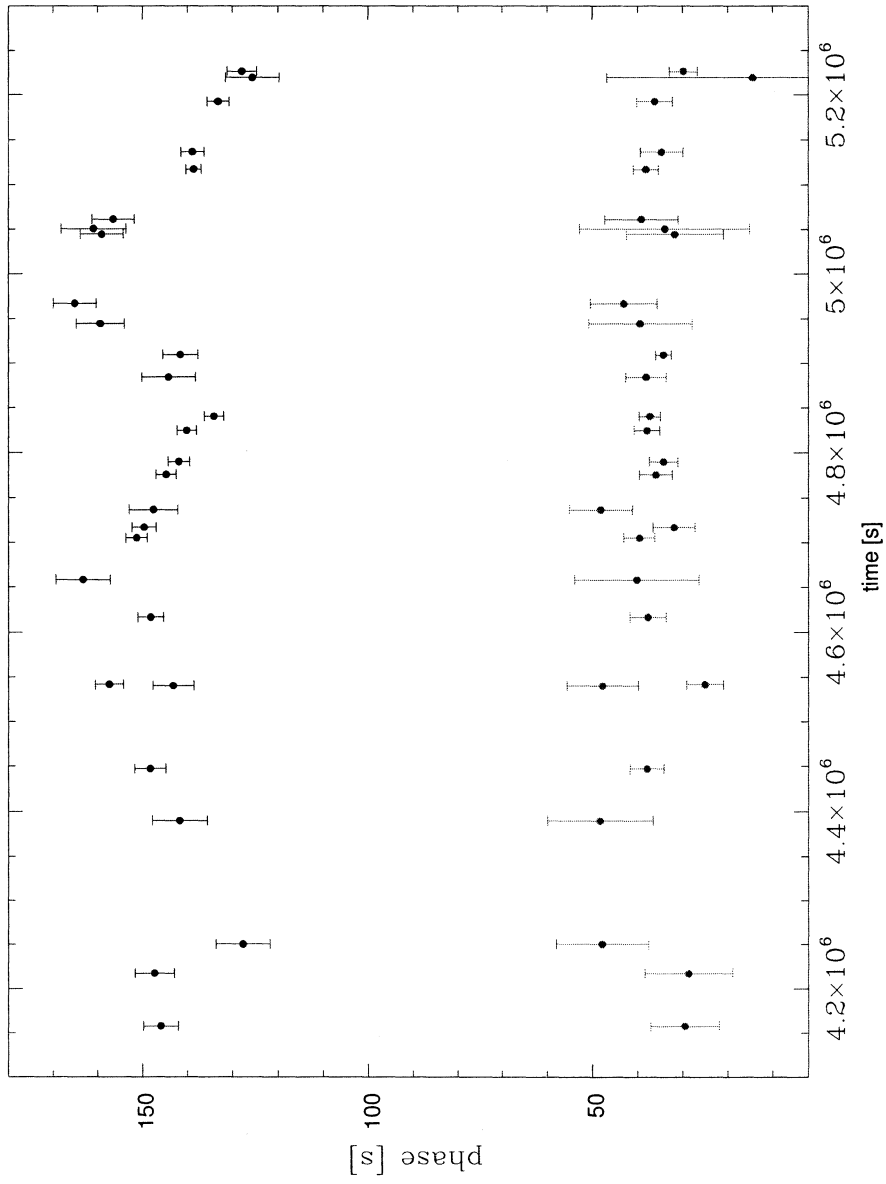

Figure 5.2 The phases of the two best resolved modes f_1 on the top and f_2 is the bottom one (in red) for each individual run.

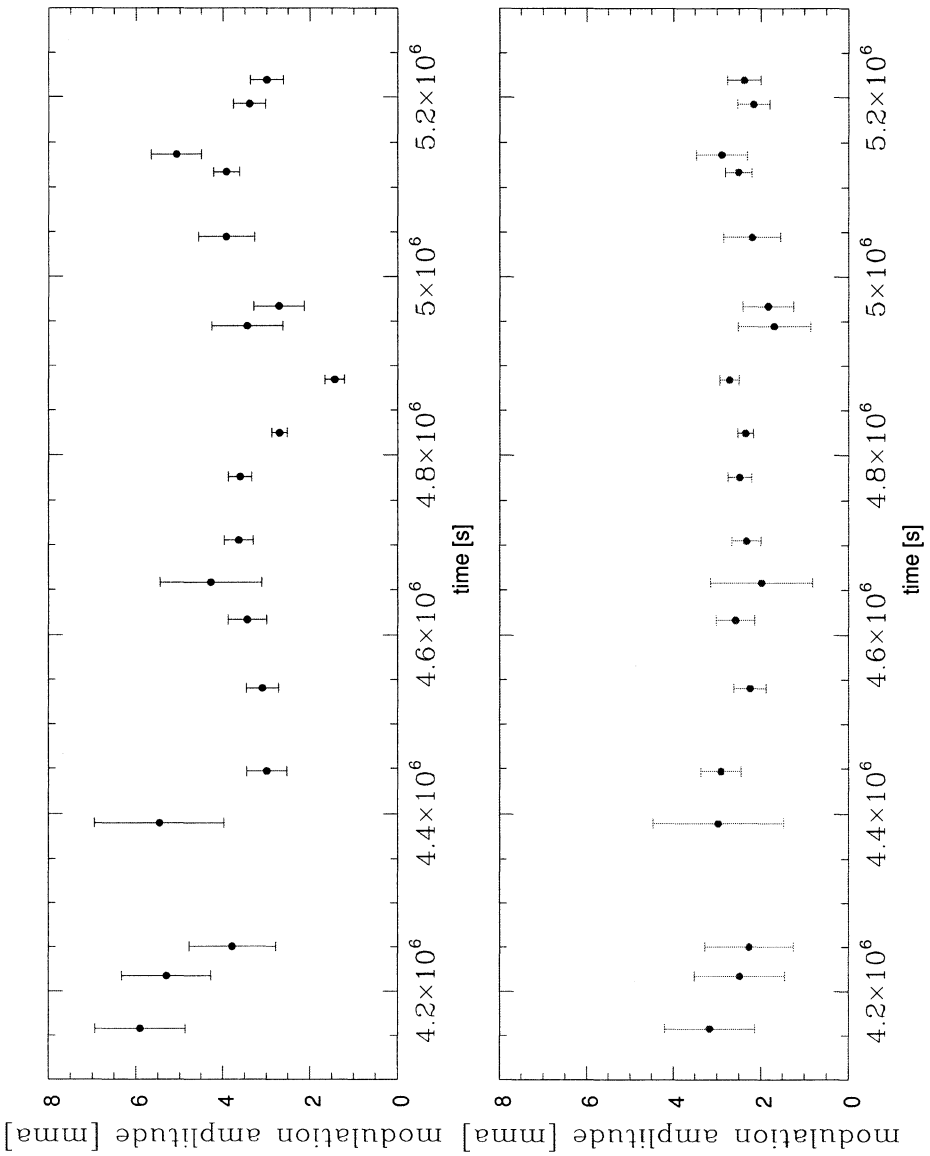

Figure 5.3 The ampitudes of the two best resolved modes f_1 on the top and f_2 is the bottom one (in red) for subsets of data.

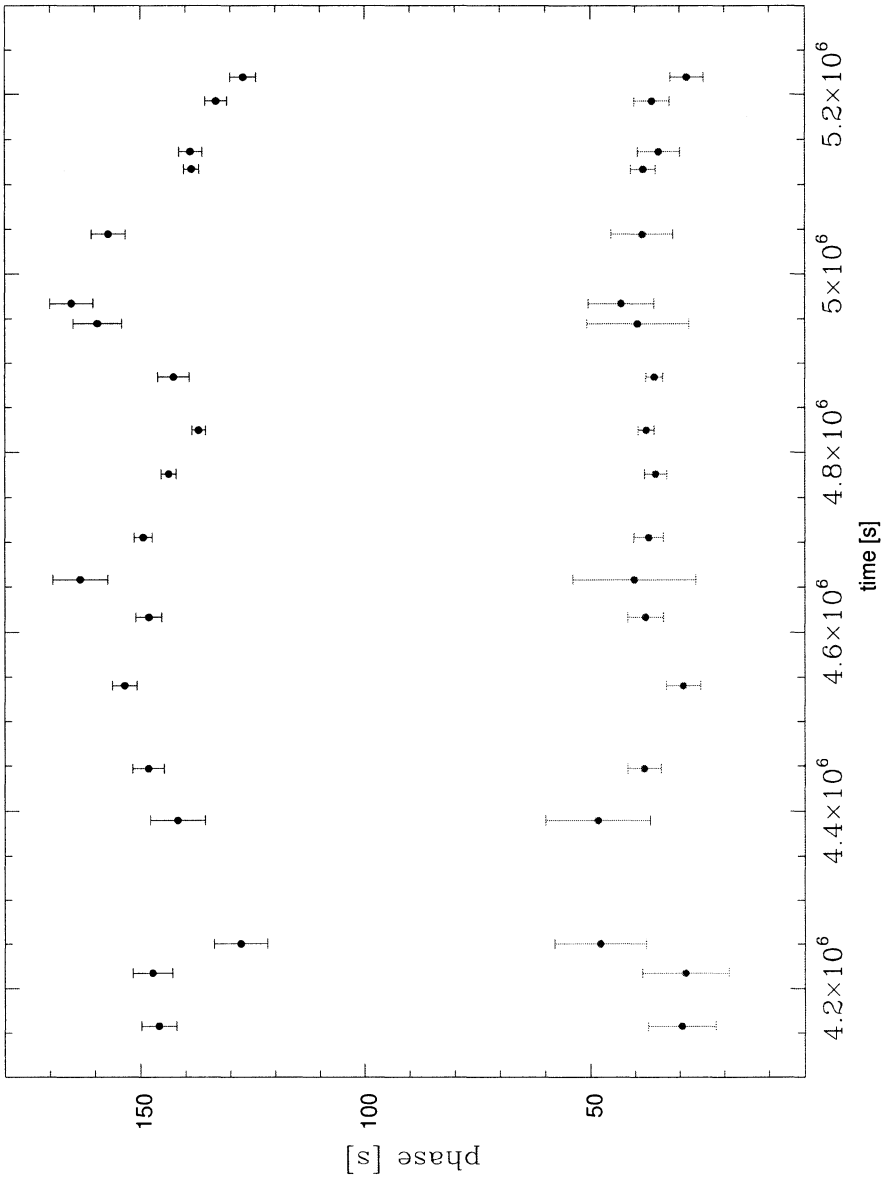

Figure 5.4 The phases of the two best resolved modes f_1 on the top and f_2 is the bottom one (in red) for the subsets of data.

of the run when the data were of very poor quality and quite sparse. All that can be said at this point is that there is a possibility of periodic change in amplitude and phase for the $f1$ mode with a period of roughly five days, likely caused by the beating of two or more closely spaced frequencies. This mode does actually have a fine structure of two or even more closely spaced modes (see Table 4.1) which supports the idea. What appears to be more certain is that the second highest peak at $f2$ is stable both in amplitude and in phase. Therefore it might be a good possible candidate for measuring the secular change of period with time, $\dot{\mathrm{P}}$.

5.2 Pattern analysis

As it is described in Chapter 2, in the asymptotic regime the non-radial $p-$modes of successive n or ℓ would appear equally spaced in frequency with modes of successive ℓ spaced half the distance of those of successive n. For the $g-$modes modes of a given ℓ should have equal period spacings with successive n. The characteristic spacings depend on the structure of the star, revealing the important parameters of the star such as the mass in the case of $g-$modes (in white dwarfs) and the radius in the case of $p-$modes. Furthermore, if the star rotates, for a given ℓ there should be $2\ell + 1$ equally spaced modes with the splitting proportional to the rotation rate of the star. Therefore, the pattern analysis is very important as it can be used for identifying the modes of pulsation and measuring stellar properties. Without a secure mode identification we cannot proceed any further into asteroseismological analysis of a star.

Unfortunately, based on standard models of sdB stars (Fontaine et al. 2001), the pulsations seen in most sdB stars are attributed to the low order, low degree $p-$modes, and as such they shouldn't show the usual asymptotic behavior, i.e. equal frequency spacing. Therefore, we cannot make use of this pattern matching technique in order to identify the modes of pulsations in these stars. But luckily stars rotate, perhaps, letting

us use the rotational splittings to identify the mode of pulsation.

Analysis of data for equally split modes that could signify rotation brought us to some rather unusual findings...

5.2.1 Numerology

At least some sdB stars have rapid rotation. Kawaler (1999) identified the five strongest modes in PG 1605+072 with the rotationaly split ℓ=1 , n=7 mode and "trapped" modes with the rotational splitting that requires the star to be rotating at 130 km/s. Heber et al. (1999) confirmed this via spectroscopy, finding that PG1605 has a significant rotation with $v \sin i$= 39 km/s. On the other hand, the theory predicts that sdB stars could have a rapidly rotating core which could be "seen" through the large rotational splittings of its non-radial modes of pulsation (Kawaler & Hostler 2005) even in stars with slow surface rotation that have small $v \sin i$. To check for any possible rotational splittings in the data we analyzed our data to see if there are any equally spaced frequencies present. Here is what we find:

Table 5.1 Possible splittings found in the WET data set on PG0014.

a [μHz]	**b** [μHz]	**c** [μHz]
$f1$ - $f2$= 262.6 $f9$ - $f10$= 259.4 $f10$ - $f7$=270.1	$f2$ - $f8$= 194.2 $f5$ - $f1$= 200.3	$f1$ - $f8$= 456.8 $f5$ - $f2$= 462.9
$\bar{a}$=264	$\bar{b}$=197.3	$\bar{c}$=460.0

These frequency intervals, in turn, show interesting ratios:

$$\sqrt{3} \cdot \bar{a} = 457.3 \approx \bar{c} \text{ to within } 1\%,$$
$$\sqrt{3}/4 \cdot \bar{c} = 199.2 \approx \bar{b} \text{ to within } 1\%.$$

This is not the first time that ratios of $\sqrt{3}$ appears in the pulsation spectrum of stars. Vauclair et al. (1996) found that the dominant modes in the amplitude spectrum of the

pulsating central star RX J2117.1+4312 show period ratios nearly exactly equal (better that 1%) with the $\sqrt{3}/2$, suggesting that the dominant peaks in this star are trapped modes. Bond et al. (1996) found that the frequency ratios of pulsating star of NGC 1501 are almost exactly $\sqrt{3}/2$ to within 1%, calling it a "magic ratio". But those stars are non-radial $g-$mode pulsators where the period spacings in the asymptotic regime scales with $\frac{1}{\sqrt{\ell(\ell+1)}}$ for a given n. Considering two $g-$modes with the same n one having ℓ =2 and ℓ =1 one can come up with the ratio of $\sqrt{3}$.

Unfortunately, we are dealing with a different type of stars! Pulsations of EC14026 stars are non-radial low order $p-$modes, based on their short periods (less than the radial fundamental) where the scaling with different n or/and ℓ **does not** depend on $\sqrt{\ell(\ell+1)}$. If, on the other hand, we assume that these frequency intervals result from the rotational splittings due to rotation, the rotation needed for such broad splittings is way too rapid. Therefore we cannot explain this numerology in the data!

5.2.2 Equal spacings

There are several ways that patterns can be found in the frequencies of PG0014+067. We note that the ($f1$, $f8$) doublet straddles the ($f5$, $f2$) doublet. Taking the centroid of each doublet we find that they are separated by 7057.6 - 6860.2 = 197.4 which is equal to spacing b in Table 5.1. While this is simply a different way to express the same spacing pattern, the difference between the centroids, spacing b, is 3/4 of spacing a.

Finding the greatest common factor between spacings a and b gives 66 μHz. Call this value δ; then spacing a is 4 times δ, and spacing b is 3 times δ. When we look at any other remaining frequency difference in our data we find frequency intervals that are nearly integral multiples of δ. We show this in Table 5.2 where we constructed a sequence of frequencies using the following empirical relation:

$$\nu_{n,m} = \nu_{in} + \delta \times n + \Delta \times m, \tag{5.1}$$

where ν_{in} is a starting value in this case ν_{in}= 5923.4 μHz, δ is a constant spacing and n is an integer, Δ is the large splitting, and m is a small integer. For the large splitting we take 1/2 of spacing c.

This phenomenological model matches all of the observed frequencies we securely identify in Chapter 4 to within 4 μHz. Furthermore, the ULTRACAM observations revealed additional secure low amplitude modes all of which fit this pattern. Table 5.3 includes those frequencies as well (we note that one of the ULTRACAM frequencies is likely a 1c/day alias based on this analysis). With all of these modes we can refine the estimate of δ to 66.7 μHz and Δ to 229 μHz. These values were used in making Tables 5.2 and 5.3.

This may seem as random thing to do so we resort to standard statistical tests used in asteroseismology to check for significance. In particular, we use the Kolmogorov-Smirnov test (KS) frequently employed in white dwarf seismology to look for equal period spacings. We also check by using an inverse variance test (IV) (Kawaler 1987, O'Donoghue 1994). Results of this analysis are shown in Figure 5.5. The results of these two tests show a very strong significance for this result - and take into account the number of independent spacings and the sizes of the gaps (see the above references for details).

Table 5.2 Spacings in PG 0014+067 from the WET run alone.

Observed μHz	Δn	Δm	**Model** μHz	**difference**
5923.4	0	0	5923.0	0.4
6193.5	4	0	6189.9	3.7
6452.9	8	0	6456.6	-3.7
6631.7	14	-1	6627.8	3.9
6826.1	17	-1	6827.9	-1.8
7088.7	14	1	7085.8	2.9
7289.0	17	1	7285.9	3.1

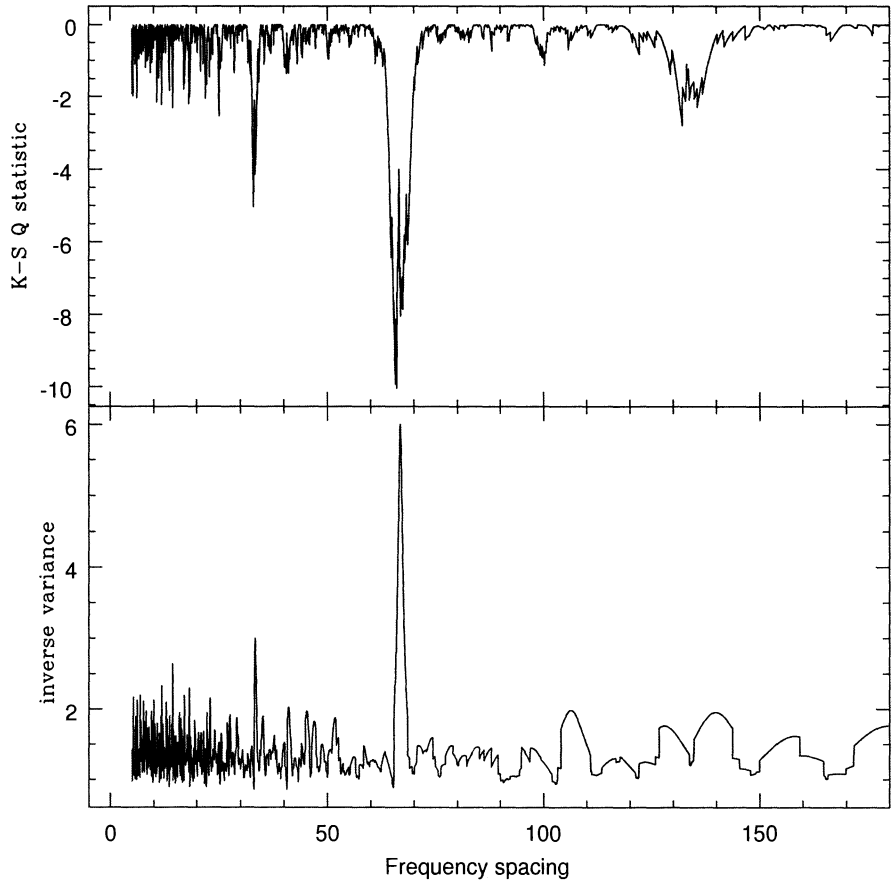

Figure 5.5 Two statistical tests for the significance of the equal frequency spacing model with δ=66.7 μHz for PG0014+067. The top shows the KS test, the bottom the IV test. Values of -10 for the Q parameter are better than any values seen in prior asteroseismological studies of compact stars.

Table 5.3 Spacings in PG 0014+067, including extra peaks from ULTRACAM.

Observed μHz	Δn	Δm	**Model** μHz	**difference**	**comment**
5780.9	-2	0	5789.6	-8.7	ULTRACAM
5923.4	0	0	5923.0	0.4	
6193.5	4	0	6189.9	3.7	
6452.9	8	0	6456.6	-3.7	
6631.7	14	-1	6627.8	3.9	
6658.1	11	0	6656.7	1.4	ULTRACAM 6646.5+1/d
6726.8	12	0	6723.4	3.4	ULTRACAM
6826.1	17	-1	6827.9	-1.8	
7088.7	14	1	7085.8	2.9	
7187.5	19	0	7190.3	-2.8	ULTRACAM
7289.0	17	1	7285.9	3.1	

Another way to proceed reveals an alternate solution of even better significance. Performing a global search within 2 parameter model on all the securely isolated frequencies we find the best model for PG0014+067 with δ=90.37 μHz, Δ = 101.22 μHz and with ν_{in}= 5923.24 μHz. Table 5.4 presents the results of this model with the 11 frequencies fitting to better than 0.05%.

The results of the statistical tests, Kolmogorov-Smirnov and 2-D inverse variance on $m = 0$ mode spacings for this model are shown in Figure 5.6. The additional peaks at $\delta/2$ and $\delta/3$ are the aliases produced by multiple peaks with the same n. These tests show a significantly higher significance level of the equal frequency spacing than the original application to PG1159 period spacings!

5.3 Can we explain all this?

No. This behavior looks just like what we would expect for high order p-mode pulsator, along with a large rotational splitting. Unfortunately, these stars ought to be low order $p-$mode pulsators based on the standard models of sdB stars. The frequencies

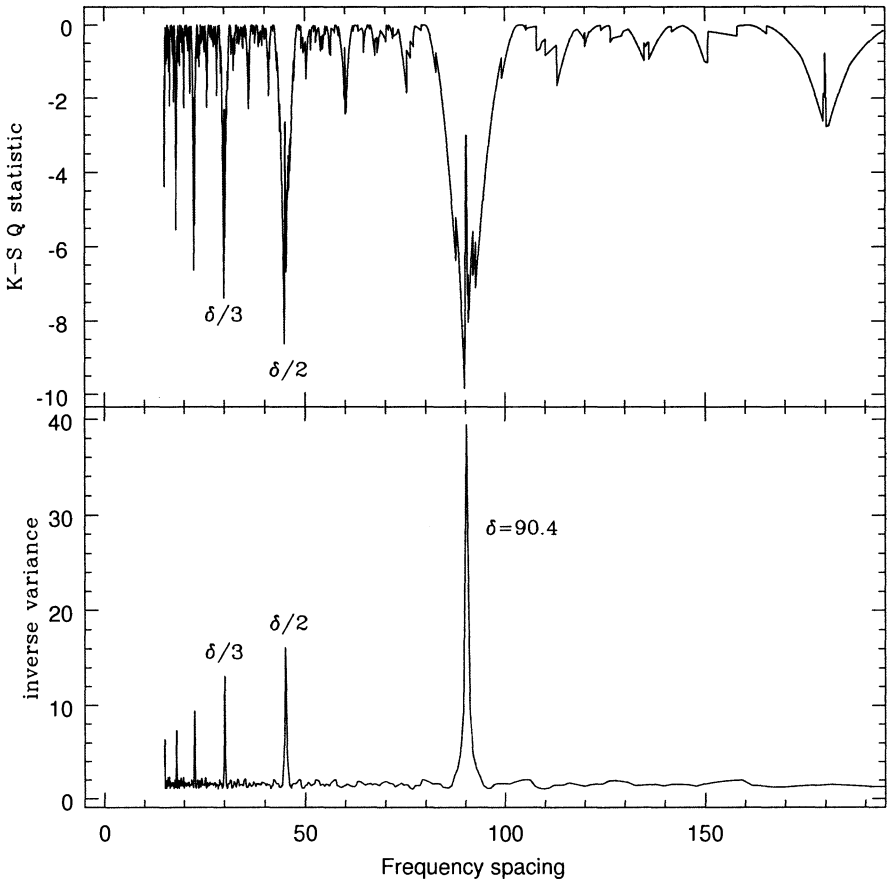

Figure 5.6 The same two statistical tests for the significance of the equal frequency spacing model with δ=90.38 μHz for PG0014+067. The top shows the KS test, the bottom the 2-D IV test.

Table 5.4 Final fit to secure modes in PG 0014+067, including the modes found in ULTRACAM data, with δ=90.37 μHz, Δ = 101.22 μHz and with ν_{in}= 5923.24 μHz.

Observed μHz	**Δn**	**Δm**	**Model** μHz	**difference**	**comment**
5923.4	0	0	5923.24	0.2	
6193.5	3	0	6194.11	-0.6	
6452.9	7	-1	6454.1	-1.2	
6632.8	9	-1	6634.6	-1.8	
6646.5	8	0	6645.6	0.9	ULTRACAM
6659.9	7	1	6656.5	-3.4	ULTRACAM white light
6726.8	10	-1	6724.9	1.9	ULTRACAM white light
6826.1	10	0	6826.1	0.0	
7088.7	14	-1	7086.1	2.6	
7187.5	14	0	7187.3	0.2	ULTRACAM
7289.0	14	1	7288.5	0.5	

we see are of order equal to the radial fundamental, given their position in the H-R diagram and the models needed to explain them. Simply put, PG0014+067 should not show what we see.

Therefore, based on what we found, either PG 0014+067 is *not* a $p-$mode pulsator, or it is a high-overtone $p-$mode pulsator and the models we have for these stars are just not correct.

One natural thing to do is to check if there is a similar pattern in other stars of the same class. Therefore, we examined four other sdB stars that have reliable frequency lists. Here we briefly summarize our findings. We find that in 4 out of the 4 (i.e. all) of the best-studied sdB stars that we sampled, the frequencies nearly all follow the same pattern. To test the significance we use the same statistical tests that we used for PG0014+067 and they show frequency spacings that are at least as significant as PG0014+067. We have not yet examined other pulsating sdB stars, because this sample of 4 are among the richest and best studied sdB stars. Other stars lack extended coverage, have too few modes or are otherwise unsuitable for this kind of analysis.

PG1047+003

Taking the frequency list from Kilkenny et al. (2002) into the Equation 5.1 we find that 10 observed frequencies fit better than 0.04% with δ= 55.86 μHz, Δ=186.46 μHz and ν_{in}= 6310.76 μHz.

PG1219+534

Taking the frequency list from Charpinet et al. (2005) we find that the observed frequencies fall into a single sequence with a common frequency spacing δ= 60.49 μHz, big spacing Δ=0 μHz and starting value ν_{in}= 5812.27 μHz. One mode out of 9 does not fit, while all the rest fit to better than 0.10%.

PB8783

Taking the frequency list from O'Donoghue et al. (1998) and Vučković et al. (2004) we find the common frequency spacing of δ= 58.05 μHz, big splitting Δ=139.85 μHz and starting value ν_{in}= 7197.8 μHz. This model fits 10 modes to better than 0.02%.

PG1336-018

Applying the Equation 5.1 to PG1336-018 with δ= 34.42 μHz, Δ=114.46 μHz, and ν_{in}= 4886.12 μHz we get the frequencies observed (taking the frequency list from Kilkenny et al. 2003) from this sequence (Equation 5.1). Interestingly, the big splitting Δ is exactly equal to the orbital period of this close binary system. This model fits 14 modes to better than 0.06%.

5.4 Summary

We find that PG0014+067 does not follow any of the expectations that theory has predicted. High ℓ modes should not show this equal frequency spacing, and rapid rotation coupled with ordinary $p-$modes cannot produce such a pattern either.

PG0014+067 is not alone. We found that at least 5 of the best-studied sdB stars, show frequencies that fall into a single sequence with a common frequency spacing.

According to the empirical relation Equation 5.1 this common frequency spacing δ is in the range of $\delta \approx$ 35-90 μHz, with the large rotational splittings $\Delta \approx$ 100-200 μHz in 4 out of 5 stars and with Δ= 0 μHz in one star (PG1219+534). The statistical tests Kolmogorov-Smirnov (KS) and inverse variance (IV) (the same statistical tests used to find equal period spacings in PG1159 stars) show positive equal frequency spacing in these stars. According to these tests (KS and IV) pulsating sdB stars have frequency spacings of higher statistical significance than the widely accepted period spacings seen in PG1159 stars. There is **only** one problem: the frequencies themselves are too small to be high-order p-modes!?

The best models of these stars have frequencies near the radial fundamental . Therefore, they are nowhere near the high-frequency range where asymptotic behavior is reasonable. Furthermore, the expected asymptotic spacing is a factor of 10 smaller than the spacing we see. The models say we should only see asymptotic $p-$mode behavior at frequencies of 30000 μHz or so, not at $\approx$5000 μHz and that the spacings should be of the order of 700 μHz.

This work started with the aim to verify the hypothesis that high ℓ modes are present in PG0014+067 and/or test the prediction of large rotational splittings caused by a rapidly rotating core, and therefore provide a valuable input into modeling the structure of this important class of evolved stars. While the outcome turned out to be negative for both theoretical expectations, one thing that was definitely confirmed is that this star is ripe for further study. We need to find the reason behind this behavior, either by revising the theoretical models, or by improving the models by incorporating other processes that can explain this equal frequency spacing we see in these stars. Are there any other modes of pulsations, available for the stars in this part of the $\log g - T_{\rm eff}$, which would lead to the their equal frequency spacing of about 35-90 μHz ? Are we seeing the "regular" $p-$modes that have been modulated by the $r-$modes?

We do not have the answers to these questions now, however one thing is certain -

nature[1] is telling us something about these stars that we are unfortunately not yet able to grasp.

[1] "Many discoveries are reserved for ages still to come, when memory of us will have been effaced. Our universe is a sorry little affair unless it has in it something for every age to investigate ... Nature does not reveal her mysteries once and for all." - Seneca, "Natural Questions", Book 7, first century.

BIBLIOGRAPHY

[Billères et al. 2002] Billères, M., Fontaine, G., Brassard, P. and Liebert, James, 2002, *ApJ, vol.578*, 515.

[Bigot et al. 2000] Bigot, L., Provost, J., Berthomien, G. and Goode, P.R., 2000, *A&A, vol.356*,p 218-233.

[Bradley et al. 1993] Bradley, P.A., Winget, D.E. and Wood, M.A., 1993, *ApJ, vol.406*, 661B.

[Brassard et al. 2001] Brassard, P., Fontaine, G., Billères, M., Charpinet, S., Liebert, James and Saffer, R.A., 2001, *ApJ, 563*, 1013.

[Bond et al. 1996] Bond, H.E., Kawaler, S.D., Ciardullo, R., Stover, R., Kuroda, T., Ishida, T., Ono, T., Tamura, S., Malasan, H., Yamasaki, A., Hashimoto, O., Kambe, E., Takeuti, M., Kato, T., Kato, M., Chen, J.-S., Leibowitz, E.M., Roth, M.M., Soffner, T. and Mitsch, W., 1996, *AJ, vol.112*(6), 2699–2711.

[Charpinet et al. 1997] Charpinet, S., Fontaine, G., Brassard, P., Chayer, P., Rogers, F.J., Iglesias, C.A. and Dorman, B. , 1997, *ApJ, 483*, L123.

[Charpinet et al. 2000] Charpinet, S., Fontaine, G., Brassard, P. and Dorman, Ben, 2000, *ApJS, 131L*, 223C.

[Charpinet et al. 2002] Charpinet, S., Fontaine, G., Brassard, P. and Dorman, Ben, 2002, *ApJS, 139*, 487C.

[Charpinet et al. 2005] Charpinet, S., Fontaine, G., Brassard, P., Green, E.M. and Chayer, P., 2005, *A&A*, *437*, 575C.

[Cox 1980] Cox, J. P., 1980, Theory of Stellar Pulsations. *Princeton: Princeton Univ. Press.*

[Cox 1974] Cox, J. P., 1974, *Reports on progress in Physics*, *vol.37*(5), 563.

[Cunha & Gough 2000] Cunha, M. and Gough, D., 2000, *MNRAS*, *vol.319*, p1020-1038.

[D'Cruz et al. 1996] D'Cruz, N.L., Dorman, B., Rood, R.T. and O'Connell, R.W., 1996, *ApJ*, *466*,359.

[Dorman et al. 1993] Dorman, B., Rood, R.T., and O'Connell, R.W., 1993, in *The Globular Cluster-Galaxy Connection ASP Conference Series, Vol.48, ed. Graeme H. Smith and Jean P. Brodie*,p553.

[Edelmann et al. 2003] Edelmann, H., Heber, U., Hagen, H.-J., Lemke, M., Dreizler, S., Napiwotzki, R. and Engels, D., 2003, *A& A*, *400*, 939E.

[Fontaine et al. 2003] Fontaine, G., Brassard, P., Charpinet, S., Green, E.M., Chayer, P., Billères, M. and Randall, S.K., 2003, *ApJ*, *vol.597*, p518-534.

[Fusi-Pecci & Renzini 1976] Fusi-Pecci, F. and Renzini, A., 1976, *A& A*, *Vol.46*, 447F.

[Greenstein & Sargent 1974] Greenstein, J.L and Sargent, A.I, 1974, *ApJS*, *Vol.28*,p157.

[Gough 1996] Gough, D.O, 1996, *The Observatory*, *vol.116*,p313-315.

[Green et al. 2003] Green, E.M., Fontaine, G., Reed, M.D., Callerame, K., Seitenzahl, I.R., White, B.A., Hyde, E.A., Østensen, R., Cordes, O., Brassard, P., Falter, S., Jeffery, E.J., Dreizler, S., Schuh, S.L., Giovanni, M., Edelmann, H., Rigby, J. and Bronowska, A., 2003, *ApJ, vol.583*,31G.

[Han et al. 2002] Han, Z., Podsiadlowski, Ph., Maxted, P.F.L., Marsh, T.R. and Ivanova, N., 2002, *MNRAS, 336*, 449H.

[Han et al. 2003] Han, Z., Podsiadlowski, Ph., Maxted, P.F.L. and Marsh, T.R., 2003, *MNRAS, 341*, 669.

[Handler 2003] Handler, G., 2003, *Baltic Astronomy, vol.12*,253-270.

[Hansen et al. 2004] Hansen, C., Kawaler, S.D. and Trimble, V., 2004, Stellar Interiors: Physical Principles, Structure and Evolution, *New York: Springer.*

[Heber et al. 1999] Heber, U., Reid, I.N., Werner, K., 1999, *A&A, vol.348*,L25-L28.

[Iben 1990] Iben, I., 1990, *ApJ, 353*, 215I.

[Jeffery et al. 2005] Jeffery, C.S., Aerts, C., Dhillon, V.S., Marsh, T.R. and Gänsicke, B.T., 2005, *MNRAS*,submitted .

[Kawaler 1986] Kawaler, S.D., 1986, *PhDT, 2K.*

[Kawaler 1987] Kawaler, S.D., 1987, *LNP, 274*,367K.

[Kawaler et al. 1999] Kawaler, S.D., Sekii, T. and Gough, D., 1999, *ApJ, 516*, 349-365.

[Kawaler & Hostler 2005] Kawaler, S.D. and Hostler, S., 2005, *ApJ, 621*, 432.

[Kawaler & Bradley 1994] Kawaler, S.D. and Bradley, P.A., 1994, *ApJ, 427*, 415K.

[Kilkenny et al. 2003] Kilkenny, D., Reed, M.D., O'Donoghue, D., Kawaler, S.D., Mukadam, A., Kleinman, S.J., Nitta, A., Metcalfe, T.S., Provencal, J.L., Watson, T.K., Sullivan, D.J., Sullivan, T., Shobbrook, R., Jiang, X.J., Joshi, S., Ashoka, B.N., Seetha, S., Leibowitz, E., Ibbetson, P., Mendelson, H., Meištas, E., Kalytis, R., Alisauskas, D., Martinez, P., van Wyk, F., Stobie, R.S., Marang, F., Zola, S., Krzesinski, J., Ogloza, W., Moskalik, P., Silvotti, R., Piccioni, A., Vauclair, G., Dolez, N., Chevreton, M., Dreizler, S., Schuh, S.L., Deetjen, J.L., Solheim, J.-E., Gonzalez Perez, J.M., Ulla, A., Østensen, R., Manteiga, M., Suarez, O., Burleigh, M., Kepler, S.O., Kanaan, A., and Giovannini, O., 2003, *MNRAS 345*, *1*,834–846.

[Kilkenny 2002] Kilkenny, D., 2002, in *ASPC: Radial and Nonradial Pulsations as Probes of Stellar Physics*, *Vol.259*, 356K, ed. Conny Aerts, Timothy R. Bedding, and Jrgen Christensen-Dalsgaard.

[Kilkenny et al. 1999] Kilkenny, D., Koen, C., O'Donoghue, D., Wyk, F. Van, Larson, K.A., Shobbrook, R., Sullivan, D.J., Burleigh, M.R., Dobbie, P.D. and Kawaler, S.D., 1999, *MNRAS*, *303*, 525K.

[Kilkenny et al. 1997] Kilkenny, D., Koen, C., O'Donoghue, D. and Stobie, R.S., 1997, *MNRAS*, *285*, 640.

[Kleinman et al. 1996] Kleinman, S.J., Nather, R.E. and Philips, T., 1996, *PASP*, *108*, 356.

[Lisker et al. 2005] Lisker, T., Heber, U., Napiwotzki, R., Christlieb, N., Han, Z., Homeier, D. and Reimers, D., 2005, *A& A*, *430*,223L.

[Maxted et al. 2001] Maxted, P.F.L., Heber, U., Marsh, T.R. and North, R.C., 2001, *MNRAS*, *vol.326*(issue4), 1391–1402.

[Maxted et al. 2004] Maxted, Pierre F.L., Morales-Rueda, L. and Marsh, T.R., 2004, *ApJ& SS, vol.291*,303M.

[Mengel et al. 1976] Mengel, J.G., Norris, J. and Gross, P.G., 1976, *ApJ, Vol.204*, 488.

[Metcalfe et al. 2005] Metcalfe, T.S., Nather, R.E., Watson, T.K., Kim, S.-L., Park, B.-G. and Handler, G., 2005, *astro-ph/0502147*.

[Mortara & Fowler 1981] Mortara, L. and Fowler, A., 2005, *SPIE. 290*,28M.

[Nather et al. 1990] Nather, R.E., Winget, D.E., Clemens, J.C., Hansen, C.J. and Hine, B.P., 1990, *ApJ. 361*,309N.

[O'Donoghue 1994] O'Donoghue, D., 1994, *MNRAS, vol.270*(2/Sept15), 222.

[O'Donoghue et al. 1998] O'Donoghue, D., Koen, C., Solheim, J.E., Barstow, M.A., Dobbie, P.D., O'Brien, M.S., Clemens, J.C., Sullivan, D.J. and Kawaler, S.D., 1998, *MNRAS, vol.296*, 296O.

[Østensen R. 2004] Østensen, R., 2004, *Ap& SS, Vol.291*, 263O.

[O'Toole et al. 2005] O'Toole, S., Jordan, S., Freidrich, S. and Heber, U., 2005, *A&A, 437*, p227-234.

[Poindexter et al. 2003] Poindexter, S., Reed, M.D., Charpinet, S. and the Whole Earth Telescope Xcov 23 team, 2003, *AAS, 203*, 1216P.

[Riddle 2003] Riddle, R., 2003, *Baltic Astronomy, 12*, 183.

[Saffer et al. 1994] Saffer, R.A., Bergeron, P. and Liebert, J., 1994, *ApJ, 432*, p351-366.

[Smeyers & Tassoul 1987] Smeyers, P. and Tassoul, M., 1987, *ApJS, 65*, p429-449.

[Tassoul 1980] Tassoul, M., 1980, *Astron.Soc. of the Pacific.Mercury, vol.9*p21.

[Tassoul 1990] Tassoul, M., 1990, *ApJ*, *vol.358*p313-327.

[Tutukov & Yungelson 1990] Tutukov, A.V. and Yungel'Son, L.R., 1990, *AZh*, *vol.67*109T.

[Unno 1990] Unno, W., 1990, *Lecture notes in Physics*, *vol.367*p103.

[Unno et al. 1989] Unno, W., Osaki, Y., Ando, H., Saio, H. and Shibahaski, H., 1989, *Nonradial oscillations of stars,* Tokyo: University of Tokyo Press 2nd ed.

[Vauclair 1996] Vauclair, G., 1996, *ASPC vol.96*397V.

[Vink 2004] Vink, J.S., 2004, *Ap& SS*, *Vol.291*, 239V.

[Vučković et al. 2004] Vučković, M., Hostler, S., Kawaler, S.D. and Behera, B., 2004, *APSP*, submitted.

[Warner 1988] Warner, B., 1988, High Speed Astronomical Photometry, *Cambrigde*

[Young 1967] Young, A.T., 1967, *AJ 72*,747.